Iranian Journal of Science and Technology, Transactions of Electrical Engineering
https://doi.org/10.1007/s40998-026-01036-z

RESEARCH PAPER

Development of A High-Performance PV Energy System Using Dingo Optimized-Fuzzy MPPT and CITSB Converter

Narayanan Rishikesh[1] · **Jeyaraj Senthil Kumar**[1] · **N. Janaki**[2]

Received: 10 April 2025 / Accepted: 4 February 2026

Abstract
This article promotes an implementation and architecture of a grid incorporated Photovoltaic (PV) energy system optimized for efficient maximum energy harvesting and grid incorporation. The proposed system incorporates a Dingo Optimized Fuzzy-Maximum Power Point Tracking (DOF-MPPT) controller for establishing optimum energy harvesting from PV within varying ecological situations. A Coupled Inductor Two-Stage Boost (CITSB) converter is utilized to amplify Direct Current (DC) voltage efficiently, while a 1Φ VSI (Voltage Source Inverter) transforms the DC to Alternating Current (AC) supply, suitable to grid injection. A Proportional-Integral (PI) controller governs reactive and actual power to ensure grid compliance with reference power demands. The MATLAB/Simulink simulations demonstrate the system's ability to extract maximum power, convert it efficaciously, and synchronize it continuously with the grid. The outcomes highlight the strength of developed system in delivering reliable and maximum efficiency (98.2%), high-quality energy to the grid while addressing the challenges of dynamic environmental conditions.

Keywords PV system · DOF-MPPT controller · Coupled inductor Two-Stage boost (CITSB) converter · VSI · LC filter and PI controller

1 Introduction

1.1 Overview

A solar connected grid system is renewable energy setup where solar panels generate electricity that is directly fed into the public utility grid (Kavin et al. 2024; Kavin et al. 2025; Badoni et al. 2021). The system consists of key components such as solar panels, an inverter, a metering system, and protection equipment (Sreedhar et al. 2025; Naqvi et al. 2020). The general architecture of PV incorporated grid structure is indicated in Fig. 1.

Solar panels transform sunlight into DC electricity, which is then transformed into AC by VSI for fulfilling the grid's frequency and voltage (Babu et al. 2020; Lakshmi et al. 2025). The electricity generated is utilized to energize the local loads, while the surplus energy is transformed to the grid, often earning credits through net metering (Ibrahim et al. 2023). When PV production is low, power is taken from the grid to establish an uninterrupted electricity delivery. PV incorporated systems are divided into three types: grid-tied without battery storage, grid-tied with battery backup, and hybrid systems that integrate multiple energy sources (Gulzar et al. 2023). These systems help reduce electricity costs, lower carbon footprints, and subsidize to a cleaner energy future (Yan et al. 2021).

1.2 Review on DC – DC Converter and MPPT Controller

Several converters are proposed by developers to enlarging the resultant voltage of solar systems. The boost converter (Veerachary and Kumar 2020) is frequently employed in booster operations owing to its substantial voltage gain, simplistic framework, low element count, increased efficiency,

✉ Narayanan Rishikesh
rishikesh@bitsathy.ac.in

[1] Department of Electrical and Electronics Engineering, Bannari Amman Institute of Technology, Erode 638401, Tamil Nadu, India

[2] Department of Electrical and Electronics Engineering, Vels Institute of Science, Technology and Advanced Studies, Pallavaram, Chennai, Tamil Nadu, India

Published online: 18 February 2026

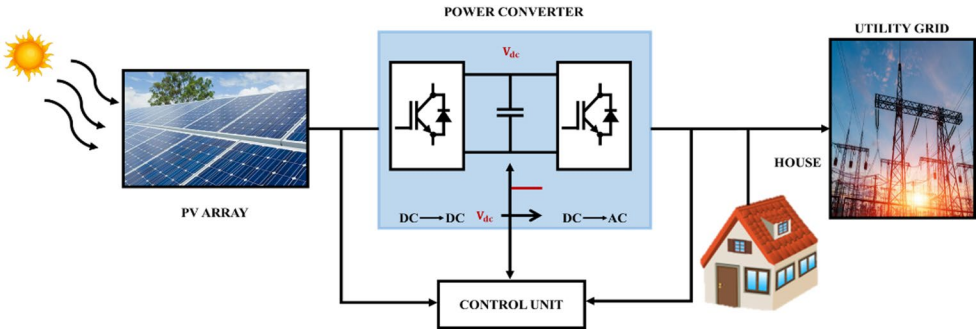

Fig. 1 Solar connected Grid System

and ease of interface with MPPT controllers. Nevertheless, it has step-up ratio limits in addition to low efficiency close to the unity duty cycle. Several methods have been proposed for converters (Wu et al. 2020) to resolve a large voltage gain and one of most popular methods is to use boost converter with SL (Switched Inductor) (Kumar et al. 2023) and boost converter with SC (Switched Capacitor) cells (Sadaf et al. 2020; Kumar et al. 2020). These converters have two different operating phases: in first phase, the cells are energized in parallel, and in second phase, they reale in series to obtain a large gain ratio. Other methods for attaining high voltage gains include boost converter employing voltage-lifting method (Kumar MA et al 2022) and Voltage Multiplier Circuit (VMC) (Mohseni et al. 2021). However, the maximal charging currents via through the converter's switch result in a substantial conduction loss in these methods. The most extensively studied of HG (High Gain) converters are CI based converters (Fan et al. 2020; Li et al. 2021; Imanlou et al. 2023). CI based converters have been applicable alternative for achieving large gains due to their simplicity and effectiveness. While some configurations are developed for HG converters (Rao and De 2023; Kokkonda and Kulkarni 2021) the energy preserved in the leakage inducer causes a switch voltage spike and reduces the converter efficiency. To overcome the aforementioned issues, active clamp circuits are presented for high step-up converters, but their conversion ratios are insufficient. The Z source integrated SC cells with Boost converter for PV applications has been developed in (Rahimi et al. 2021), which substantially reduce the stress voltage on switch, but the voltage gain isn't satisfactory. A single switch buck boost converter for stepping the resultant voltage PV panel is implemented in (Dhimish and Schofield 2022), that performs well in the varying ecological conditions with reduced conversion efficiency. An improved switched inductor configuration-based Boost topology is designed in (Bao et al. 2021) that employs the double switch for attaining a greater gain ratio while reducing the amount of reactive components whereas preserving a comparable amount of semiconductor components. However, the configuration size is increased by a substantial number of passive components. In (Khan et al. 2021), a Modern Transformer-Free Ultra High Gain based Boost converter is introduced. Its single switch facilitates the way it works. However, the stress profile of the converter is high among diode and switch. The reference (Shanthi et al. 2021) proposes a Boost converter with one switching impedance topology. This two-stage converter features minimal switch loss and increased efficiency with maximum conduction loss when operating at high output voltage. The article proposes an efficient CITSB converter with maximum conversion efficiency ratio to overcome these issues.

It is necessary to improve each component of PV system to raise the energy conversion efficiency. Under various climatic conditions, a MPPT controller has been employed for strengthening panel's output (Sorte et al. 2021). A common method to MPPT is Perturbation and Observation (P&O) tactic because of its ease of use and simplicity (Bhattacharyya et al. 2020). But with this approach, there are an abundance of variations around the MPP, which leads to a high-power loss, especially in large-scale PV system. In ref (Gupta et al. 2020; Mishra and Tiwari 2021) develops the Incremental Conductance (INC) approach as a solution to these issues. Through the measurement of the spontaneous conductance to INC variables of panel power, this method is ability of tracing the Maximum Power Point (MPP) over time. The tracing effectiveness under various conditions has been greatly enhanced by the use of artificial intelligence approaches for MPPT, including neural networks (Kiran et al. 2020), and Fuzzy Logic Controller (FLC) based MPPT (Kurian et al. 2022), in comparison to traditional methods. The FLCs are intelligent systems that are insensitive to changes in topology, parameters, and operating circumstances, in contrast to linear controllers. System designers find the FLC appealing because of these features. FLCs design challenges include the discovering the inference systems of fuzzy, the range and shape of changes in fuzzy rules and membership functions. In order to overcome these challenges, these rules and membership functions need to be tuned in terms of their shape and range of changes. To optimize FLC parameters, heuristic techniques including Particle Swarm Optimization (PSO) (Firdausi et al. 2020), Multiverse Optimization Algorithm (MOA) (Venkatanarayana and Rosalina 2024),

Genetic Algorithm (GA) (Mohammed et al. 2021), Gradient Optimization (GO) (Rezk et al. 2023), Bat optimized FLC (Ali et al. 2022), Simulated Annealing Optimization (SAO) (Zhang et al. 2022) and Grey Wolf Optimization (GWO) (Laxman et al. 2021) have been proposed in recent years. These methods are efficiently enhancing the system performance by effectively searching for optimal parameter values, reducing manual tuning efforts, and improving adaptability to dynamic environments. Despite their efficiency, heuristic optimization methods might have problems with convergence, either becoming trapped in local optima or requiring an excessive amount of processing power for achieving to the global optimum. Therefore, this article presents a new Dingo Optimization for tuning the parameters of FLC to achieve improved results in MPP.

1.3 Research Motivation and Novelty

The primary motive behind this study is ongoing inability of traditional PV grid-connected systems to achieve optimal energy extraction under dynamic operating conditions. The architecture's capacity to continuously operate at the MPP is often hampered by voltage instability, higher power losses, and poor adaptation to sudden changes in temperature and sun irradiation. These difficulties underscore the necessity for a sophisticated control approach that provides the increased accuracy, quicker dynamic response, and reliable performance.

The establishment of a sophisticated optimization framework that cleverly adjusts crucial system parameters to improve tracking accuracy and conversion efficiency which makes this study unique. The proposed methodology, in contrast to conventional techniques, greatly increases system adaptability and reduces power regulation inefficiencies under changing atmospheric conditions.

1.4 Contribution of the Research

- An advanced optimization framework to enhance the power conversion efficiency of PV grid incorporated systems, minimizing energy losses and ensuring stable operation.
- The developed CITSB converter enhances voltage gain whereas decreasing stress on switching device and conduction losses, strengthen the efficacy and stability of PV-grid incorporated connected systems.
- Dingo tuned FLC based MPPT controller achieves faster and more accurate MPP with enhanced adaptability and decreased oscillations at changing environmental circumstances, ensuring optimal energy harvesting.

1.5 Organization of Paper

This paper is arranged as follow as: section II explains the description of developed system, section III explains the overall modelling of developed system, section IV explains the obtained outcomes of developed research work and finally, the entire proposed work is concluded in section V.

2 Proposed System Description

Traditional grid-connected PV systems suffer from inefficient MPPT, low voltage gain, and poor grid synchronization. Conventional MPPT algorithms exhibit slow convergence and oscillations, while standard boost converters have limited voltage gain. To address these issues, this article introduces a Dingo Optimized-Fuzzy MPPT improves tracking efficiency and CITSB converter enhances voltage gain as showcased in Fig. 2.

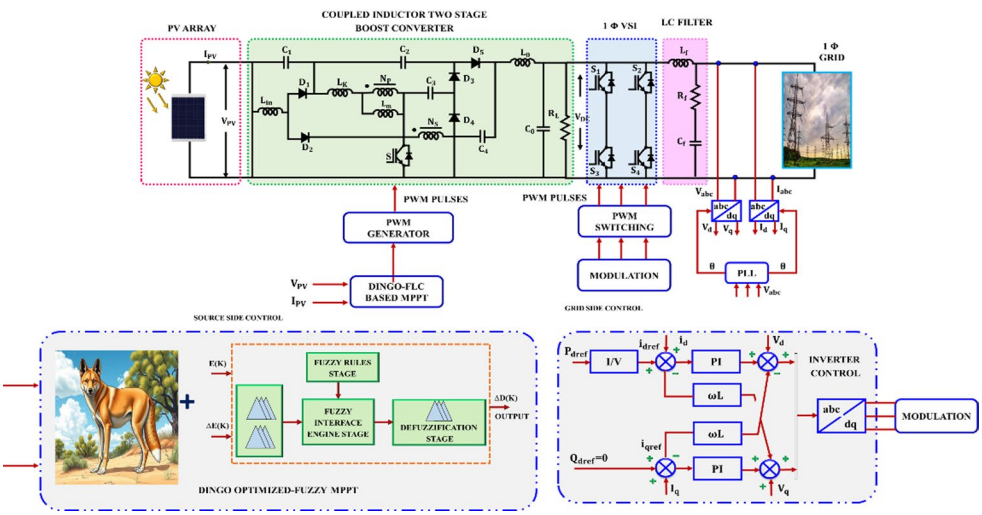

Fig. 2 Performance Enhancement of PV incorporated Grid System deploying DOA with FLC-MPPT Controller

The PV system produces a DC voltage (V_{pv}) and current (I_{pv}) based on solar irradiation, which are fed into the MPPT controller. The DOF MPPT enhances the efficacy of energy extraction by dynamically adjusting the duty factor of CITSB converter. The generated duty factor is used by PWM generator to control the CITSB, which enhance the panel voltage to a consistent dc link voltage. This high-gain converter improves energy conversion efficiency. The 1Φ VSI then transforms a regulated DC into AC power suitable for grid connection. This system ensures optimal energy utilization, improved power quality, and seamless combination of panel power into the grid whenever maintaining voltage stability and synchronization.

3 Proposed System Modelling

3.1 Modelling of Panel

A cell's equivalent circuit of PV must be modelled in order to comprehend its behavior and generate effective PV systems. The single diode model is most extensively utilized analogues circuitry model for a photovoltaic cell.

The PV cell is shown in this model as a desirable source of current connected in linked with a resistor and a diode (Fig. 3). The following are the calculations for the single diode model (Rasheed and Shihab 2020):

$$\begin{aligned} I &= I_{ph} - I_s\left(\exp\left(\tfrac{q(V+R_aI)}{N_sKTa}\right)-1\right) - \tfrac{V+R_aI}{R_b} \\ \{ \quad &: I_{PV} = \tfrac{G}{G_r}[I_{pvn} + K_1(T-T_r) \\ &: I_s = \tfrac{I_{scn}+K_1(T-T_r)}{\exp(V_{ocr}+K_V(T-T_r)/a(N_sKT)-1)} \end{aligned} \tag{1}$$

The following formula provides output current of PV array's.

$$I = I_{ph} - I_oN_{pp}[\exp\left(V + \frac{R_a\left(\frac{N_{ss}}{N_{pp}}\right)I}{V_TaN_{ss}} - 1\right) - \frac{V + R_a\left(\frac{N_{ss}}{N_{pp}}\right)I}{R_b\left(\frac{N_{ss}}{N_{pp}}\right)} \tag{2}$$

where I symbolizes the array current, I_{ph} for photo current and I_o for reverse saturation current. The voltage is indicated through V, and thermal by V_T, a is diode ideality factor. Cell parallel and series resistance are symbolized by R_b and R_a. The no. of modules in parallel and series is indicated as N_{pp} and N_{ss}. A electron charge is denoted by q, Boltzmann constant, denoted by k. The following section provides the clear explanation of CITSB converter to enlarge resultant voltage of panel.

3.2 Coupled Inductor Two Stage Boost Converter

The output voltage PV panel is enhanced with maximal gain ratio deploying CITSB converter. Figure 4 displays the circuitry illustration for the developed CITSB converter. A PV source input (V_{PV}), a switch (S), a coupled inductor, capacitors and diodes make up the converter. Additionally, the outcome is subjected to a resistant load.

A following assumption are made to understand the developed configuration:

- Since the capacitors in the converter are extensive enough, the voltages across all of components have been thought to be stable to a one time period.
- With the allowance of linked inductor that considers a leakage inductance, every component is perfect.

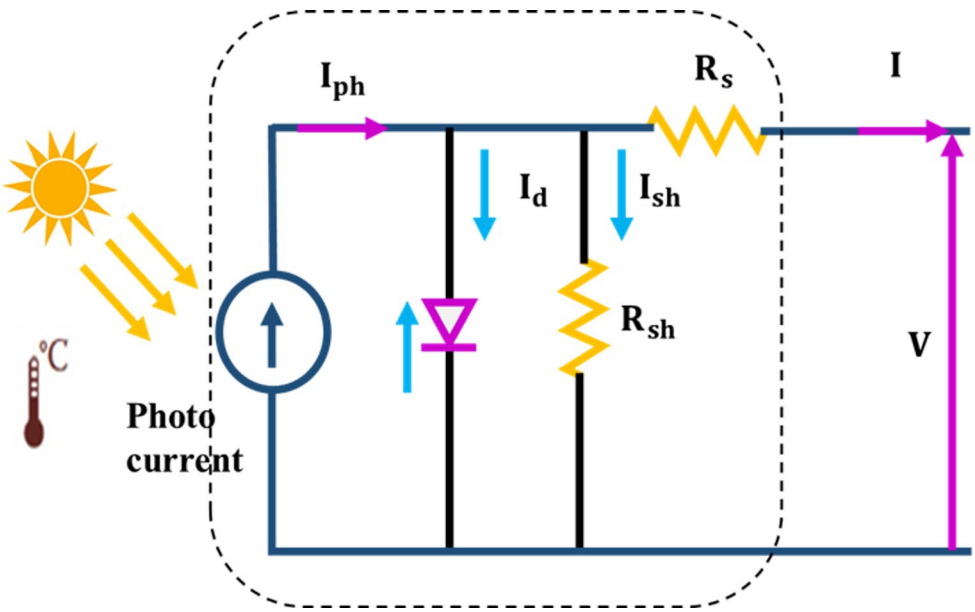

Fig. 3 PV Analogues Circuitry

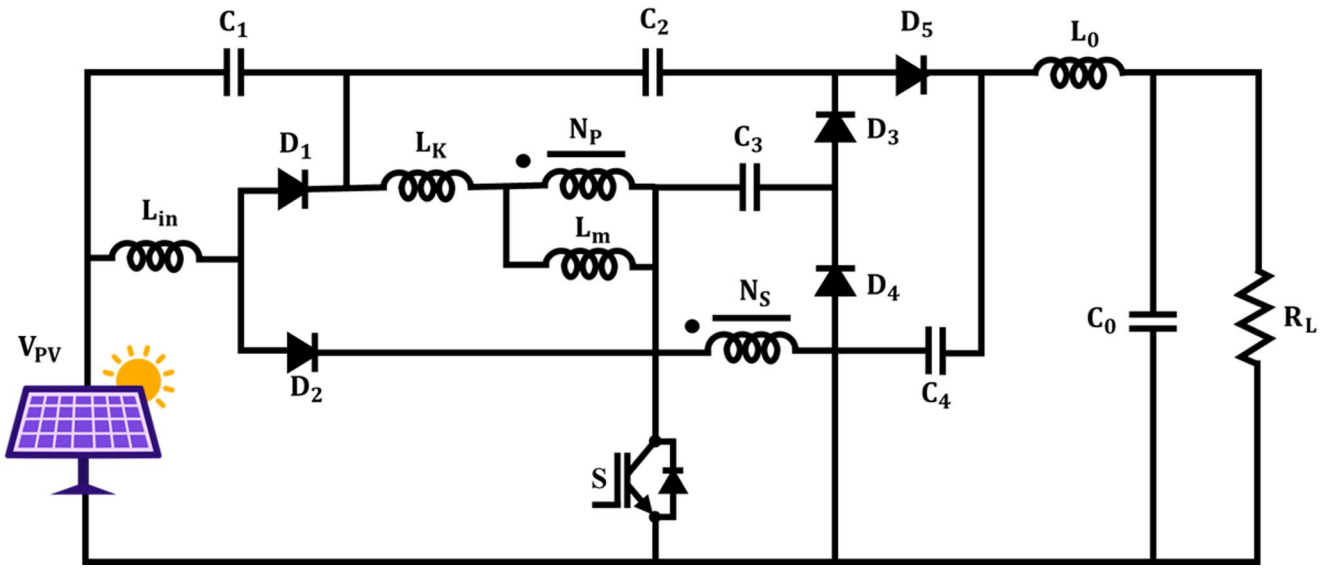

Fig. 4 Designed CITSB Converter

The designed configuration working in CCM, which consists of different phase in a only one transient duration. Figure 5 displays the operating modes of the CITSB coonverter. Figure 6 shows conceptual waveforms of the proposed converter. The following is an explanation of the operating stages:

Mode 1 $[t_o < t < t_1]$ The toggle S and diodes D_2, D_4 are activated at this time. This incoming source charges the inductances, L_m, L_k and L_{in}. The load gets a releasing from the output capacitor. Whereas inductance currents iL_k as well as iL_m balance, this state stops.

Mode 2 $[t_1 < t < t_2]$ Here, the S and D_2 and D_5 activated. Using input sources, the inductance L_{in}, L_k and L_m are gets energized. The current in secondary side of linked inductor energizes C_4, and energy is then preserved in capacitors C_1 and C_2. The R_L is powered through the C_o and to exit this state, flip off switch.

Mode 3 $[t_2 < t < t_3]$: Toggle S is off state in this stage and D_1, D_3, and D_5 diodes are activated. Here, a linear decrease in leaking inducer current. Inductance $L_{in}$is responsible for charging capacitor C_1. Capacitor C_4 gets the released energy from capacitors C_2 and C_3.

Mode 4 $[t_3 < t < t_4]$: This phase starts from D_1 and D_3 are activated throughout this period. Diode D_3 demagnetizes the leaking inductor to capacitor C_2. The is C_o energized by the linked inductor passing through output L_o. Capacitors C_3 and C_4 discharge to the C_o and capacitor C_2, correspondingly. When diode D_3 is deactivated, this phase stops.

Mode 5 $[t_4 < t < t_5]$: Here, the D_1 and D_4 are activated in this state. Inductor L_{in} and coupled inductor, correspondingly, energized capacitors C_1 and C_3. Here, a continuous decrease in magnetized and leaking inductor currents. The load receives the discharge of capacitor C_4. For leaving this mode, flip switch S back on.

3.2.1 Steady State Analysis

Since Modes one and three are significantly briefer than these time intervals, only Modes 2, 4, and 5 are taken into consideration to streamline the steady-state evaluation. Furthermore, the study ignores the CIs leakage inductance.

In state 2, the switch is activated, and the coupled inductance and $L_{in}$are energized through the incoming source. Figure 6(b) indicates that the forthcoming expressions are valid:

$$V_{Lin} = V_I \tag{3}$$

$$V_{Lm} = V_I + V_{C1} \tag{4}$$

In state 4 and 5, the voltage between inductance V_{Lin} is attained as,

$$V_{Lin} = -V_{C1} \tag{5}$$

Mode 4 allows one to acquire the voltage between the inductor V_{Lm} as,

$$V_{Lm} = V_{C3} - V_{C2} \tag{6}$$

In stage 4, the capacitor voltage expression is found as:

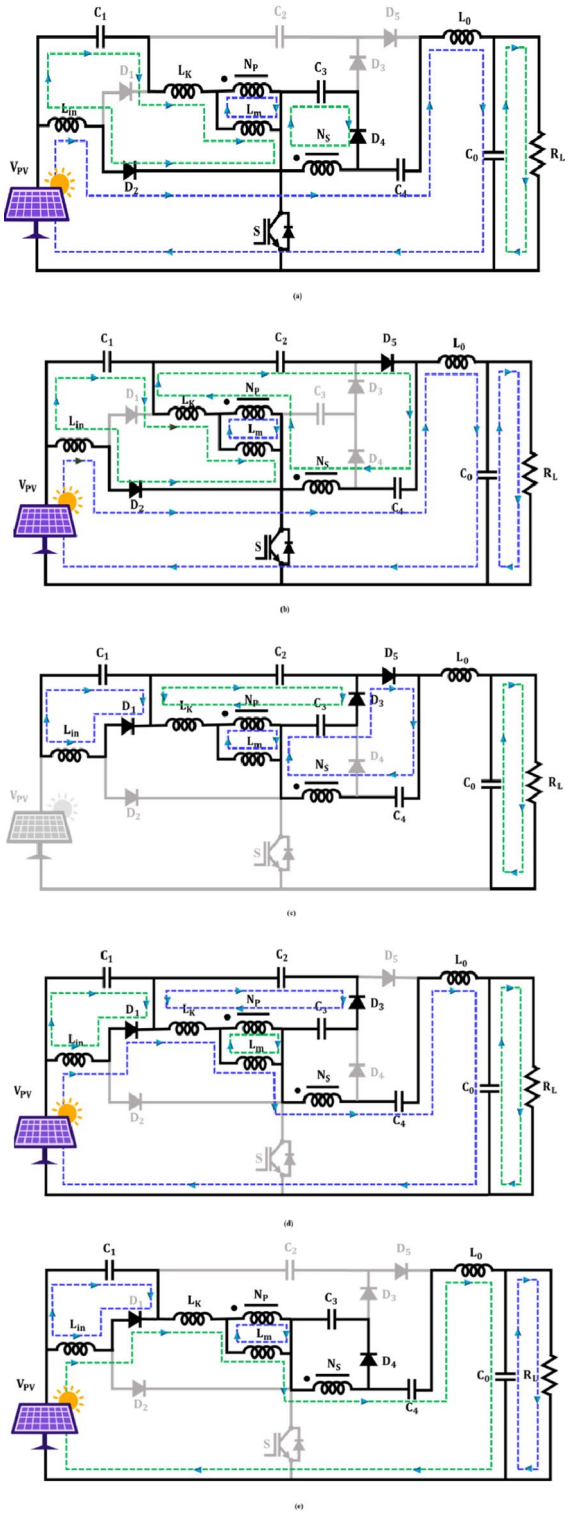

Fig. 5 Operational Modes of CITSB converter

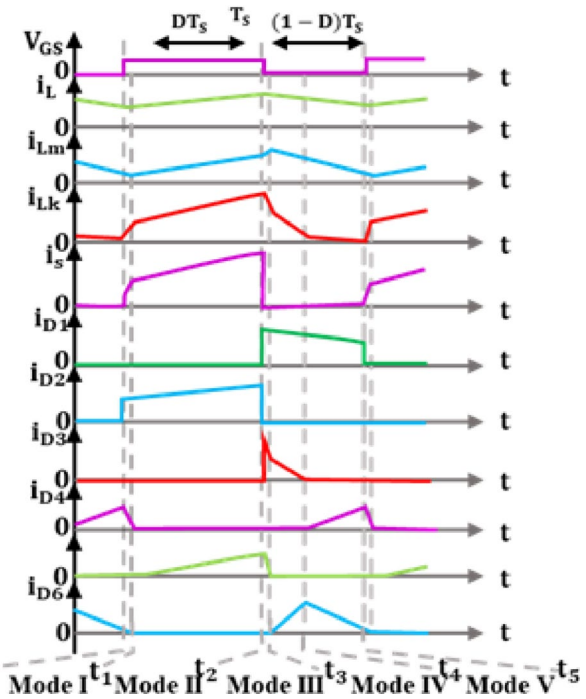

Fig. 6 Conceptual Waveform of CITSB Converter

$$V_o = V_I + V_{C1} + V_{C4} + (n+1)(V_{C2} - V_{C3}) \tag{7}$$

where n is the coupled-inductor N_s/N_s turn ratio. In Mode 5, the voltage among the inductance L_m is written as,

$$V_{Lm} = -\frac{V_{C3}}{n} \tag{8}$$

The formula for voltage of capacitor is found in Mode 5 by ignoring the voltage among the leaking inductor as,

$$V_o = V_{C4} + V_I + V_{C1} + V_{C3} + \frac{1}{n}V_{C3} \tag{9}$$

Equations (7) and (9) are equivalent since it is believed that the capacitors are large enough, which results in,

$$nV_{c2} = (n+1)V_{C3} \tag{10}$$

By converting (10) into (8) and streamlining the formulas, the magnetized inductor L_m voltage in state 5 is written as,

$$V_{Lm} = V_{C3} - V_{C2} \tag{11}$$

The C_1 voltage has been established by inserting the volt-second balance concept to inductance L_{in} in accordance with (3) and (5).

$$V_{c1} = \frac{D}{1-D} V_I \tag{12}$$

Equations (4), (6), and (11) is used to apply the same idea to the inductor L_m, yielding the given results:

$$D\,(V_I + V_{C1}) + (1-D)\,(V_{C3} - V_{C2}) = 0 \tag{13}$$

Calculating the voltage value of C_2 and C_3 by integrating (10) and (12) into (13),

$$V_{c2} = \frac{D(n+1)}{1-D^2} V_I \tag{14}$$

$$V_{c3} = \frac{nD}{1-D^2} V_I \tag{15}$$

The capacitor voltage of C_4 in Mode 2 is attained employing the following expression:

$$V_{c4} = V_{c2} + V_{c1} + V_I + n(V_{c1} + V_I) \tag{16}$$

The C_4 voltage is found by entering (12) and (14) into the equation above.

$$V_{c4} = \frac{n+1}{1-D^2} V_I \tag{17}$$

Furthermore, the gain ratio of developed circuitry is attained by utilizing (9) and the capacitor voltages:

$$M_{CCM} = \frac{V_o}{V_I} = \frac{2+n+nD}{1-D^2} \tag{18}$$

The designed converter accomplishes maximum voltage gain with conversion ratio in the context of enhancing the voltage of panel. However, the power production of solar modules is nonlinear, making it extremely difficult to obtain peak power from sunlight-dependent systems. In this research, a DOF-MPPT is designed to collect the greatest amount of power from clean energy resources.

3.3 Modelling of Dingo Optimized Fuzzy Based MPPT Controller

An intelligent system termed the Dingo adjusted Fuzzy-MPPT approach is developed to enlarge a PV panel's power output in a variety of atmospheric circumstances. The PV panel starts the process by providing the controller with real-time electrical signals, namely voltage and current, which are inputs. A FLC, which is made to deal with the non-linear and dynamic characteristics of solar energy systems, receives these values continuously. The Fuzzy Controller (FC) employs a rule basis derived from expert knowledge to interpret the change in voltage (ΔV) and change in power (ΔP) into language variables, such as "increase," "decrease," or "steady."

3.3.1 Fuzzy Logic Controller

The FLC is capable of controlling nonlinear systems and lacks sophisticated mathematical procedures as seen in Fig. 7. The exact configuration of the FLC parameters, which are established through trial and error, determines the controller behavior. Three steps form the foundation of fuzzy logic control design and implementation (Aly and Rezk 2021):

- Fuzzification.
- Finding the fuzzy rules.
- Defuzzification.

Membership functions are deployed to transform the fuzzy values into sharp values during the fuzzification stage.

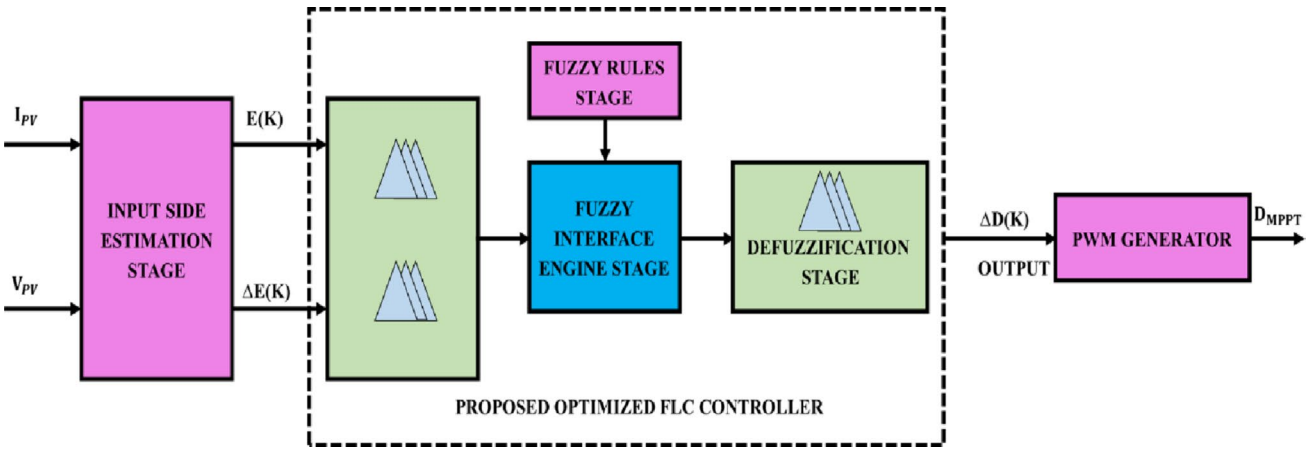

Fig. 7 FLC Structure

Using "if-then" rules, the fuzzy inference engine transforms input into output. A defuzzification procedure transforms a FC outcome parameter into a crisp one. In the PV systems, the FC's input is slope of $I_{PV}\ vs\ V_{PV}$ curve. The FLC input variables are detailed by the upcoming expressions:

$$E(k) = \frac{p(k) - p(k-1)}{v(k) - v(k-1)} \tag{19}$$

$$\Delta E(k) = E(k) - E(k-1) \tag{20}$$

Furthermore, the resultant parameter as,

$$\Delta D(k) = p(k) - p(k-1) \tag{21}$$

Here, a $p(k)$and $v(k)$ stands for the panel's power and voltage at moment k, correspondingly. FLC uses Membership Functions (MFs) and a rule table being utilized in conjunction with these two inputs to select the next OP. The FLC employs derivative method as efficient simplified technique to lessen the noise impact, often takes fluctuations in current and voltage as inputs.

Triangular MFs are popular in fuzzy logic controllers because of their simple mathematical structure, which allows for fast computation and minimal storage demands. This feature is especially critical for MPPT algorithms, which necessitate rapid decision-making to monitor the MPP under constantly changing temperature and irradiance settings. The employment of symmetric MFs around the zero-error zone ensures consistent sensitivity for both positive and negative deviations, resulting in a seamless and steady control behavior while switching between operational points. Such symmetry eliminates sudden duty-cycle changes and steady oscillations around the MPP, leading in increased controller stability. Furthermore, the overlap among neighbouring triangular MFs promotes efficient fuzzification and defuzzification processes, increasing convergence speed and decreasing tracking error. In summary, the proposed MF structure works well for MPPT control because it provides resilient performance, fast dynamic response, and consistent stability while requiring minimal computationally overhead, which renders it suitable for both simulation and execution in hardware.

The objective function of maximum power generation in a dingo optimized fuzzy based MPPT controller is expressed as,

$$\max_{\theta}\ J(\theta) = \max_{\theta}\ P_{PV}(k) \tag{22}$$

Where,

$$P_{PV}(k) = V_{PV}(k)\, I_{PV}(k) \tag{23}$$

Here, solar array current and voltage are symbolized by the $V_{PV}(k)$ and $I_{PV}(k)$ at sampling instant k and o represents the set of fuzzy controller parameters optimized by the dingo algorithm (input/output scaling factors, MF parameters and rule weights).

The outputs of FLCs are usually changes in the duty factor ΔD. In general, the number of MFs has an impact on the system's accuracy and speed. The input and output MFs in Fig. 8 are represented by the linguistic variables $PH,\ PL,\ NL, NH,\ and\ EZ$, which stand for Positive High, Positive Low, Negative Low, Negative High, and Error Zero, accordingly. The fuzzy rule foundation consists of a "if-then" rule set that includes all the data required to regulate controller settings. The fuzzy inference rules are made up of MFs for each input, are shown in Table 1.

The gating signals are determined by the controller once it gets the panel current and voltage. The MPPT system uses the current and voltage to produce the voltage command ($V*$). For establishing the MPP, the developed approach regulates the V_{PV} drawn from the PV array and employs feedback for the output voltage. To enlarge the convergence speed and tracking accuracy of MPPT process, the Dingo Optimization approach is employed rule set parameters to and tuning the MFs of FC system.

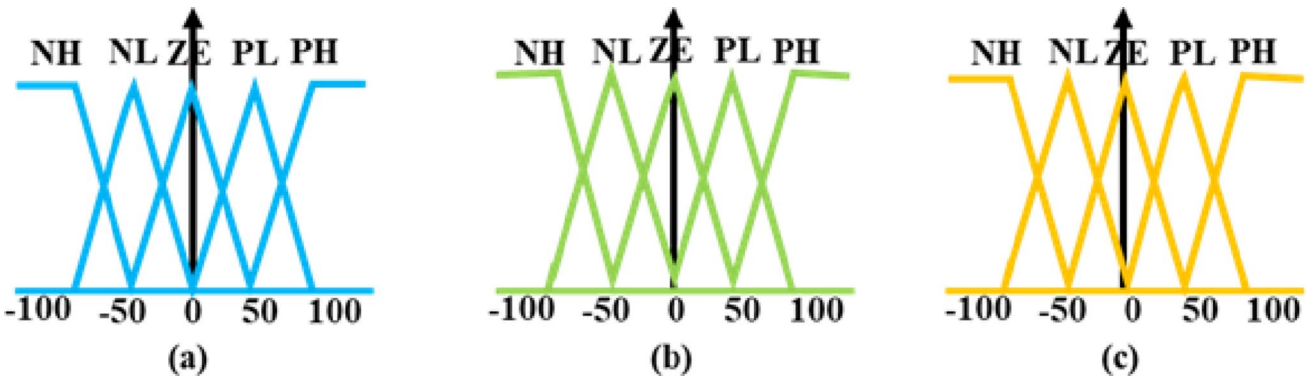

Fig. 8 Input and Output of FLC MFs

Table 1 Fuzzy rules

$\Delta e(k)$ / $e(k)$	NH	NL	ZE	PL	PH
NH	NH	NH	NL	NH	NH
NL	NH	NL	NL	NL	NH
ZE	NL	NL	ZE	PL	PL
PL	PH	PL	PL	PL	PH
PH	PH	PH	PL	PH	PH

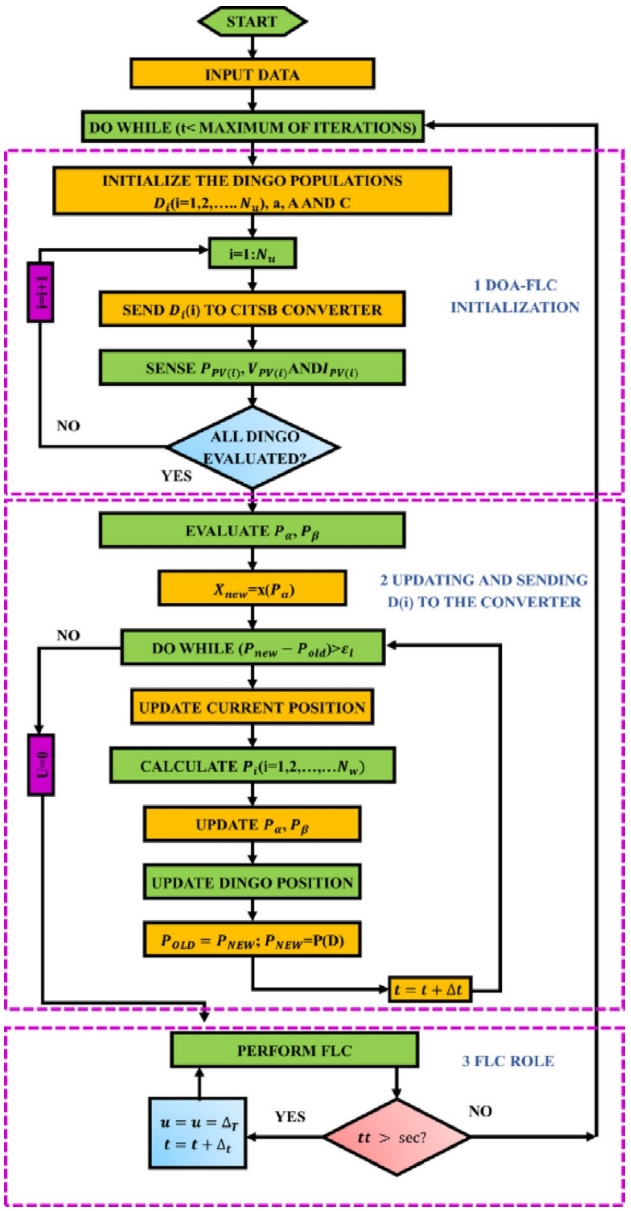

Fig. 9 DOA Tuned FLC based MPPT Controller Flowchart

3.3.2 Dingo Optimization Algorithm

Dingo optimization is inspired by the cooperative and survival behaviours of wild dingoes, this algorithm efficiently explores the solution space and fine-tunes the fuzzy controller to adapt to changing PV conditions as seen in Fig. 9. The dingo's physiological identity, wolf dingo is subsequently modified from Canis familiaris (dog) and dingoes are complex, intelligent and gregarious creatures. It is the scouts' responsibility to watch over the territory and warn the group of any dangerous situations. One of the more intriguing social behaviours of dingoes is group hunting, which increases their social activity (Bairwa et al. 2021). Hunting tactics are divided into the following phases:

- Chasing.
- Encircling.
- Attack.

The dingo optimization is carried out through the mathematical design of the modelling of the hunting, encircling, and attacking prey.

3.3.3 Encircling

Dingo's recognize their prey with sufficient ability and once the pack has located the prey, alpha follows and encircles it. The following mathematical formulas (24)–(28) characterize the behavior of dingo.

$$\overrightarrow{D_d} = \left| \overrightarrow{A}.\overrightarrow{P_p}(x) - \overrightarrow{P}(i) \right|, \tag{24}$$

$$\overrightarrow{P}(i+1) = \overrightarrow{P_p}(x) - \overrightarrow{B}.\overrightarrow{D}(d), \tag{25}$$

$$\overrightarrow{A} = 2.\overrightarrow{a_1}, \tag{26}$$

$$\overrightarrow{B} = 2.\overrightarrow{b}.\overrightarrow{a_2} - \overrightarrow{b}, \tag{27}$$

$$\overrightarrow{b} = 3 - \left(I * \left(\frac{3}{I_{max}} \right) \right) \tag{28}$$

3.3.4 Hunting

Depending on the hunting perception, and negotiators typically do not calculate the prey's position (optimal) in the search space. All of the pack individuals, such as α, β, and remain dingo's, have a thorough comprehension of possible

position of prey, according to the statistical layout of dingoes' hunting strategy. Equations (29)–(34) are the models in this concern, based on the discussion.

$$\overrightarrow{D_a} = |\overrightarrow{A_1}.\overrightarrow{P_p} - \overrightarrow{P}| \tag{29}$$

$$\overrightarrow{D}_\beta = |\overrightarrow{A_2}.\overrightarrow{P_\beta} - \overrightarrow{P}| \tag{30}$$

$$\overrightarrow{D}_o = |\overrightarrow{A_3}.\overrightarrow{P_o} - \overrightarrow{P}| \tag{31}$$

$$\overrightarrow{P_1} = \left|\overrightarrow{P_\alpha} - \overrightarrow{B}.\overrightarrow{D_a}\right| \tag{32}$$

$$\overrightarrow{P_2} = \left|\overrightarrow{P_\beta} - \overrightarrow{B}.\overrightarrow{D_\beta}\right| \tag{33}$$

$$\overrightarrow{P_3} = \left|\overrightarrow{P_o} - \overrightarrow{B}.\overrightarrow{D_o}\right| \tag{34}$$

The subsequent formulas are deployed to determine every dingo's strength:

$$\overrightarrow{\mathrm{I}_a} = \log\left(\frac{1}{F_a - (1E-100)} + 1\right) \tag{35}$$

$$\overrightarrow{\mathrm{I}_\beta} = \log\left(\frac{1}{F_\beta - (1E-100)} + 1\right), \tag{36}$$

$$\overrightarrow{\mathrm{I}_o} = \log\left(\frac{1}{F_o - (1E-100)} + 1\right) \tag{37}$$

3.3.5 Attacking

If there fails to be a location update, the dingo attacked the victim to end the hunt. The technique is mathematically formulated by decreasing the value of $\overrightarrow{b}$ in a linear fashion. A search agent's updated location could be among its current position and prey's location when randomized values of $\overrightarrow{D_a}$ are in (Kavin et al. 2024, Kavin et al. 2024).

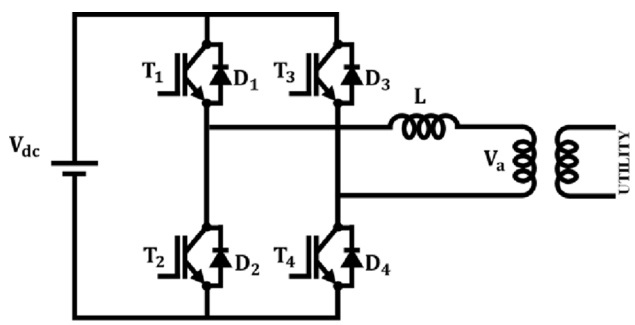

Fig. 10 — 1Φ VSI

3.3.6 Searching

Dingo's hunt mostly according to the location of the group. They constantly go onward in attack and search carnivore. Thus, $\overrightarrow{B}$ is used for randomized values; a value greater than one denotes that the pack is approaching the prey, whereas a value smaller than minus one denotes that the prey is moving away from the search agent.

3.4 Single Phase VSI Modelling

The topology of 1Φ VSI is depicted in Fig. 10. Four diodes ($D1$, $D2$, $D3$, $and\ D4$), Four power switches ($T1$, $T2$, $T3$, $and\ T4$) and a dc voltage source make up this device. Utilizing a step-up transformer and filter inductor L, the inverter output has been attached to grid (Azab 2021).

Grid synchronization using a PI controller is employed for integrating PV system, into the power grid. The PI controller establishes that output frequency and voltage of the inverter are accurately aligned with the grid parameters, enabling seamless and stable power transfer. It continuously monitors the phase angle, frequency, and amplitude of grid and modify the inverter's outcome accordingly. By minimizing the error among actual and reference grid signals, the PI controller maintains synchronization and reduces disturbances during grid fluctuations.

3.5 LC Filter Design

An LC filter has been constructed at the inverter output to eliminate high frequency switching harmonics produced by the inverter and guarantee grid code compliance. The fundamental grid frequency pass through the LC filter with minimal distortion while switching-frequency components are effectively attenuated (Xue et al. 2024).

3.5.1 Inductor Selection

The filter inductance L_f is chosen based on the allowable current ripple ΔI:

$$L_f = \frac{V_{dc}}{6 f_s \Delta I} \tag{38}$$

Where, the V_{dc} is dc link voltage, f_s is the inverter switching frequency and $\Delta I$is the permissible current ripple.

3.5.2 Capacitor Selection

To reduce voltage ripple and reactive power injection, the filter capacitance C_f is chosen:

$$C_f \leq \frac{Q_c}{\omega_g V_g^2} \tag{39}$$

Where, Q_c is allowable reactive power, $\omega_g = 2\pi f_g$ is grid angular frequency and V_g is grid voltage.

3.5.3 Resonant Frequency Constraint

The resonant frequency of the LC filter, fr is selected so that:

$$10 f_g < f_r = \frac{1}{2\pi \sqrt{L_f, C_f}} < 0.1 f_s \tag{40}$$

This guarantees sufficient harmonic attenuation and avoidance of grid frequency resonance.

4 Results and Discussion

For improving PV tied utility grid performance, this article presents a fresh DOF based MPPT controller with CITSB converter. This section elaborates the attained results of designed work. Table 2 indicates the components description of developed work.

4.1 Test Case Condition 1

Figure 11 illustrates the input waveforms of panel, specifically highlighting the temp and solar irradiance profiles under the conditions of Test Case 1. As observed from the Fig. 11, both parameters remain constant throughout the test duration. The temp is bolstered at a steady value of $35^\circ C$, w the panel irradiance is consistently held at $1000\, W/m^2$.

Figure 12 presents the output voltage of PV panel and corresponding input current waveform of the CITSB converter under Test Case 1. As shown, the regulated and held steady voltage is approximately 120 V, indicating effective MPPT performance. Simultaneously, the converter input current remains stable around 52 A, reflecting consistent power extraction from the PV source. Minor distortions observed in the current waveform are attributed to switching dynamics and transient response of the converter; however, they are within acceptable limits and isn't affect the entire efficacy of system.

Figure 13 indicates the output waveforms of CITSB converter using a DOA-tuned fuzzy MPPT controller under Test Case 1. The converter successfully preserves a consistent output voltage of 400 V and current of 13 A, assuring the efficacy of controller in regulating power. Meanwhile, the corresponding output and input power waveforms demonstrate that the system quickly reaches and sustains a stable power level. This highlights the reliability and efficiency of the DOA-fuzzy MPPT in dynamic operating conditions.

4.2 Test Case Condition 2

The testing conditions of panel are demonstrated under a consistent temp and a varying irradiance profile, as illustrated in the Fig. 14. Throughout the test, the temperature is consistently maintained at 35°C to isolate the impact of solar intensity variations. The irradiance levels are varied

Table 2 Parameter Specifications

Solar PV System		DOA-FUZZY controller	
Parameters	Values	Parameters	Values
$open\ circuit\ Voltage\ V_{oc}$	37.25 V	$Input\ Membership\ Functions$	5
$Maximum\ Voltage\ V_m$	29.95 V	$Population\ Size(P)$	50
$Parallel\ Connected\ Solar\ cell$	15	$Output\ MFs$	5
$Series\ connected\ Solar\ cell$	3	$Maximum\ Iterations$	50
$Maximum\ Current\ I_m$	8.35 A	$No.\ of\ search\ agents$	2
$Short\ circuit\ Current\ I_{oc}$	8.95 A	$Rules\ Ratio$	25 (5×5)
CITSB Converter			
Winding 1			
$N_p\ (H)$		$1.1\ mH$	
$R_p\ (ohm)$		1.1	
Winding 2			
$N_s\ (H)$		$1.1\ mH$	
$R_s\ (ohm)$		1.1	
C_1, C_2, C_3, C_4		$4.7\mu\ F$	
C_o		$2200\mu\ F$	
Switching Frequency		10 kHz	

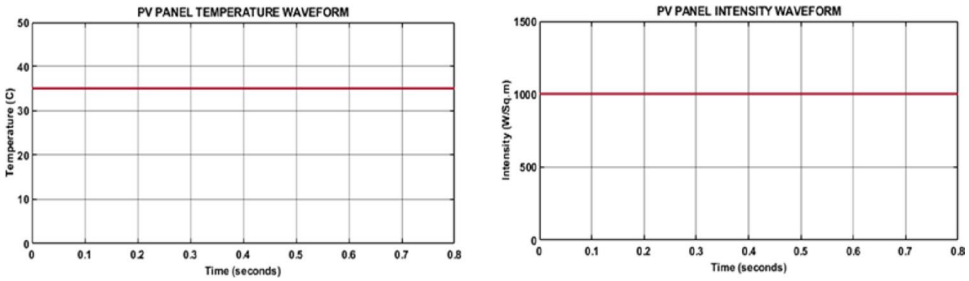

Fig. 11 Panel Profile under Test Case 1

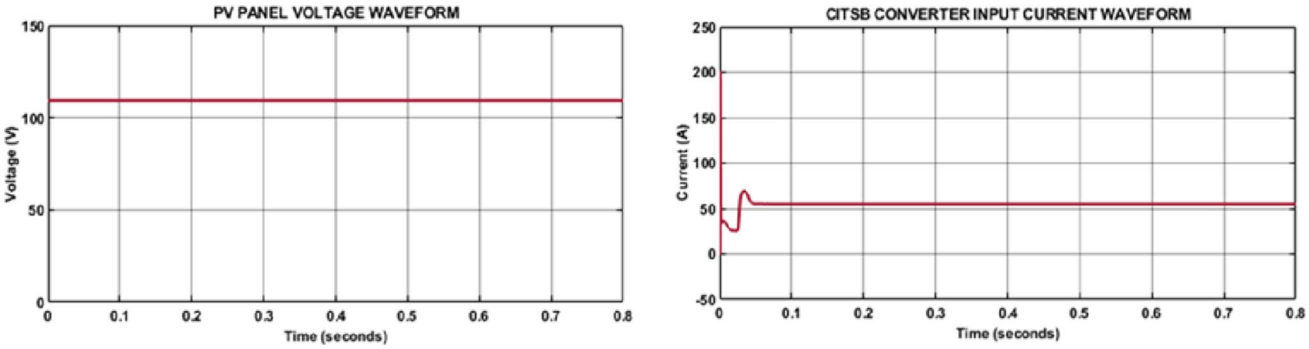

Fig. 12 PV Output Profile Waveform at Test Case 1

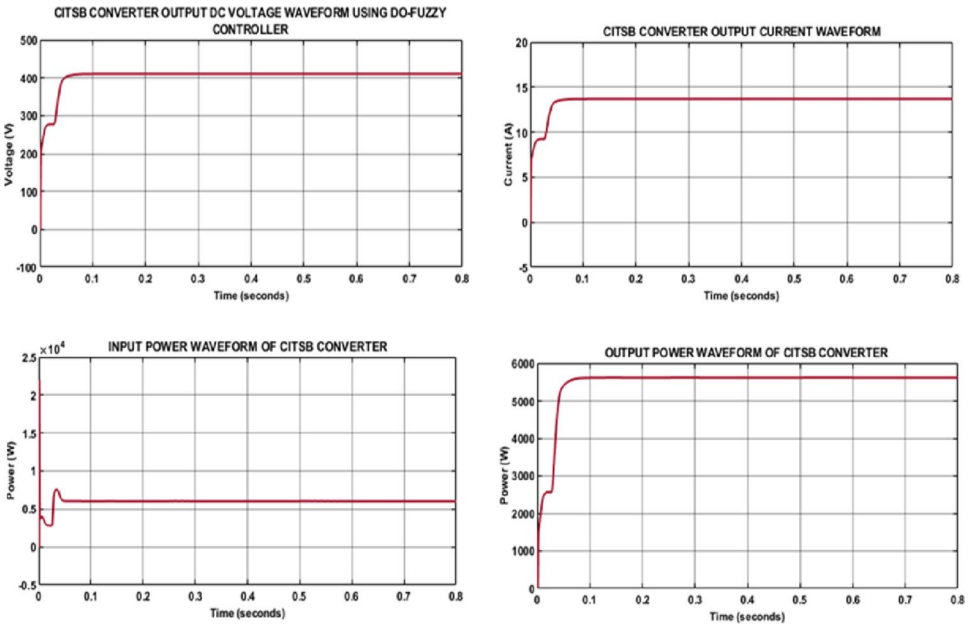

Fig. 13 Converter Output Profile and Power at Test Case 1

from 900 W/m² to 1000 W/m², simulating realistic changes in sunlight exposure.

The output profile value of panel and CITSB converter waveform under test case 2 condition is showcased in Fig. 15. From the Figure illustration, is it clear that the panel preserves 120 V after the certain periods of seconds and the current maintain slightly distorted 52 A value accordingly.

Under Test Case 2, the CITSB converter's output profile waveforms deploying a DOA-tuned fuzzy MPPT controller are shown in the Fig. 16. After 0.6, the converter reliably sustains a steady output voltage of 400 V and current of 13 A, demonstrating the controller's ability to effectively control energy. The matching profile power waveforms also show the speed at which the system reaches and maintains a steady power level. This demonstrates the DOA-fuzzy MPPT's dependability and effectiveness under changing operating circumstances.

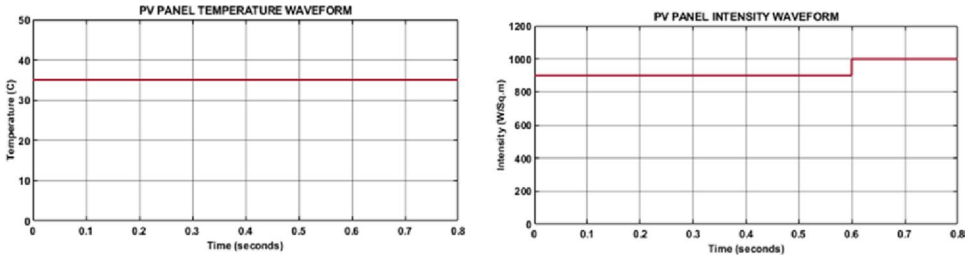

Fig. 14 PV Panel Temperature and Intensity Under Test Case 2

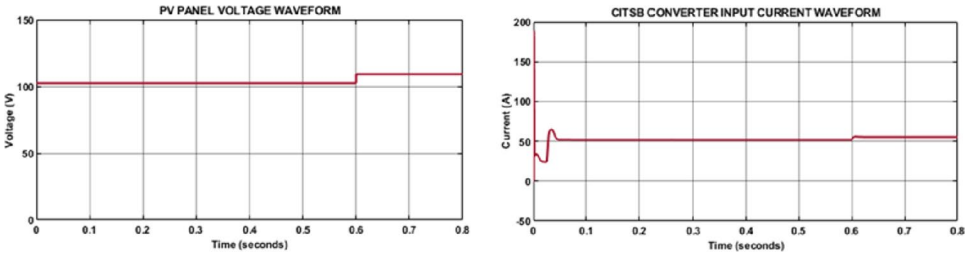

Fig. 15 PV Profile Waveform under Test Case 2

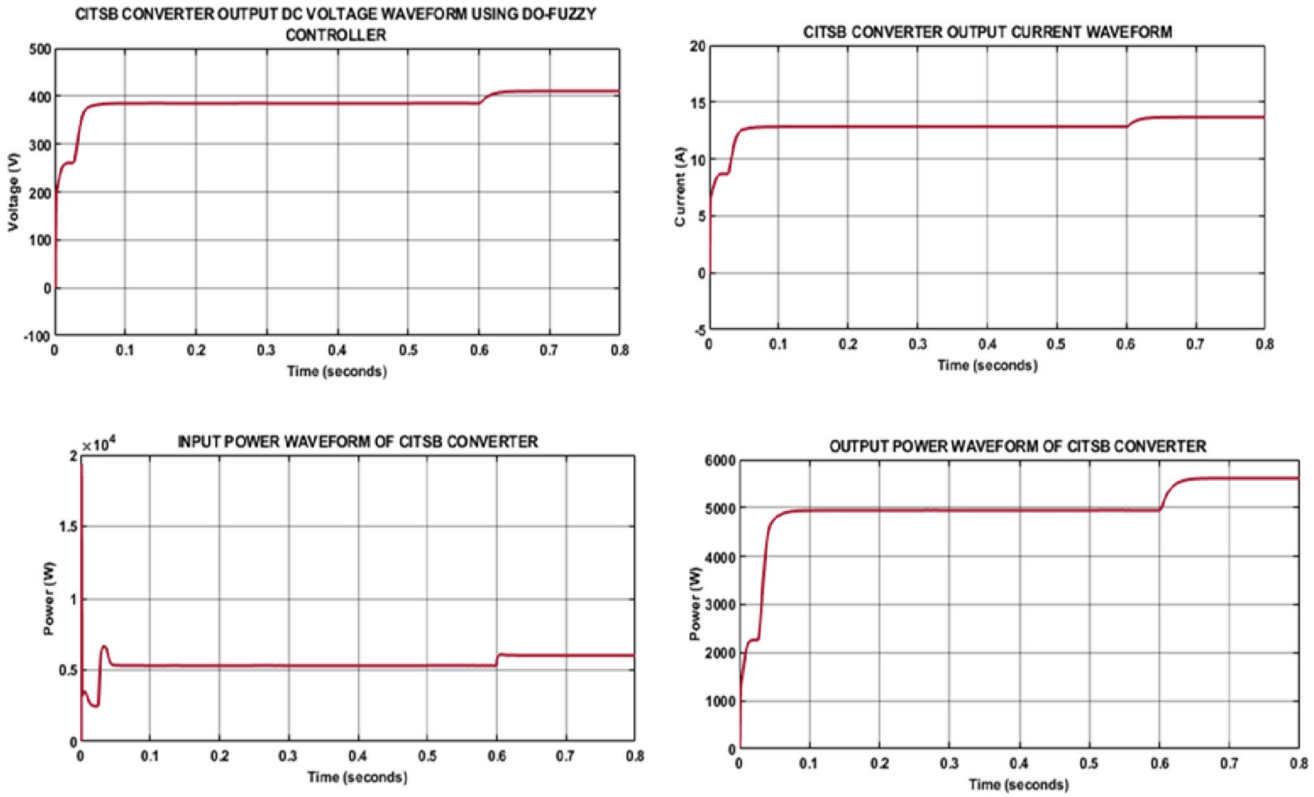

Fig. 16 Converter Output and Power Waveform Under Test Case 2

4.3 Case 3: Changing Temperature & Varying Intensity

The testing case condition 3 panel input waveforms under changing intensity and temperature waveforms are illustrated in Fig. 17. In this scenario, the intensity value is ranging from $900\,w/sq.m\,to\,1000\,w/sq.m$ and temperature value ranging from $25?\,to\,35?$ are attained accordingly.

Figure 18 denotes the PV panel output profile waveform under test case 3 condition. Here, the panel voltage maintains the 120 V after short period of times due to the variations in intensity and temperature. Likewise, the CITSB converter input current value 52 A value is obtained with minimized distortions.

The profile waveforms of the CITSB converter utilizing a DOF-MPPT controller are denoted in the Fig. 19 under Test Case 3. The converter consistently sustains a constant

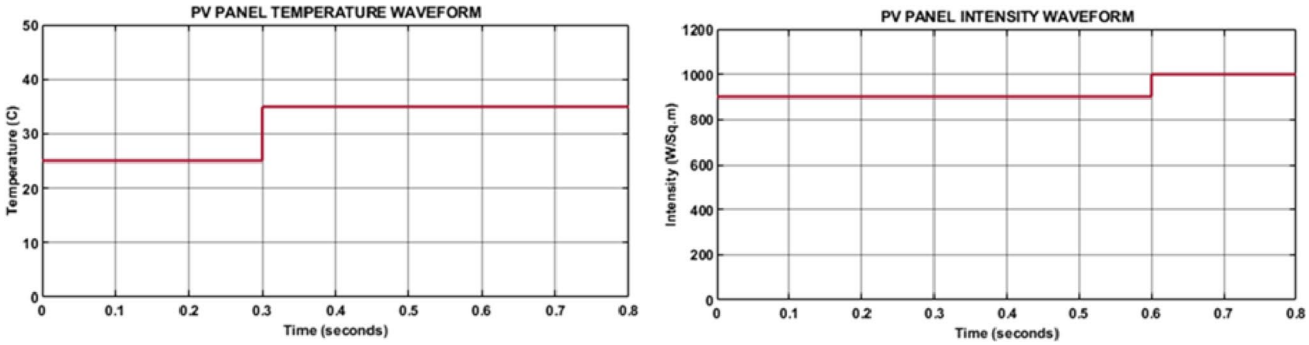

Fig. 17 Panel Profile Under Test Case 3

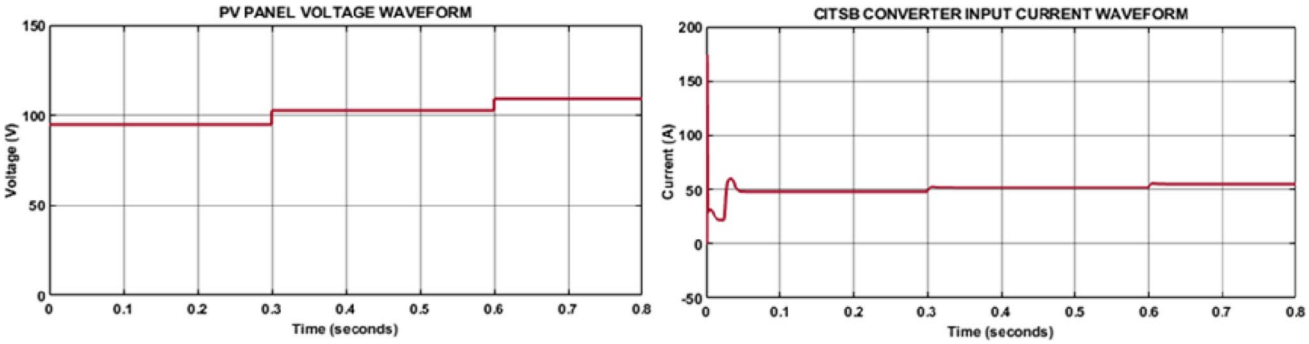

Fig. 18 PV Panel Output Profile Waveform Under Test Case 3

400 V and 13 A after the specified amount of time, proving the controller's capacity to efficiently manage power. The pace at which the system achieves and sustains a constant power level is also displayed by the corresponding power waveforms. This illustrates a dependability and efficacy of the DOA-fuzzy MPPT in dynamic operation conditions.

4.4 Case 4: Under Partial Shading Conditions

The panel functioning circumstances within partial shadowing, where the temp is kept almost consistent at 35 °C for the length of test, are shown in Fig. 20. In order to simulate shading effects, the sun irradiance first stays at $1000\ \boldsymbol{W/m^2}$ and then decreases to about $800\ \boldsymbol{W/m^2}$at 0.6 s. Effective dynamic responsiveness is demonstrated with PV voltage dropping from $110\ \boldsymbol{V\ to}\ 95\ \boldsymbol{V}$ and the converter input current stabilizing at 50 A.

The effectiveness of the CITSB converter under partial shadowing is showcased in Fig. 21. After the irradiance drops at 0.6 s, the output DC voltage quickly increases to roughly 400 V within 0.6 s and settles close to 360 V. During shade, the output current is significantly reduced to 12 A from its regulated value of 14 A. As a result, the output power first approaches 5600 W and then stabilizes at about 4300 W, indicating successful regulation.

4.5 Grid Performance Under 1500 W

The grid performance under a 1500 W power supply is depicted in the Fig. 22, demonstrating stable and efficient operation. The system maintains a consistent voltage of 230 V and a current of approximately 12 A. The real power delivered to the grid (1500 W) remains stable, indicating effective power transfer with minimal losses. Additionally, the reactive power observed is negligible, which highlights proper power factor correction and minimal reactive component in the current. Figure 23 indicates the output THD waveform under 1500 W power supply grid condition, which indicates that the THD has reduced value of 2.91%.

4.6 Grid Performance Under 2000 W

Figure 24 shows the grid's performance under a 2000 W power source, showing steady and effective operation. The system consistently maintains a current of about 12 A and a grid voltage of 230 V. Effective power transfer with low losses is demonstrated by the steady real power (2000 W) supplied to the grid. Furthermore, there is very little reactive power present, indicating adequate power factor correction and a low reactive component in the current. The

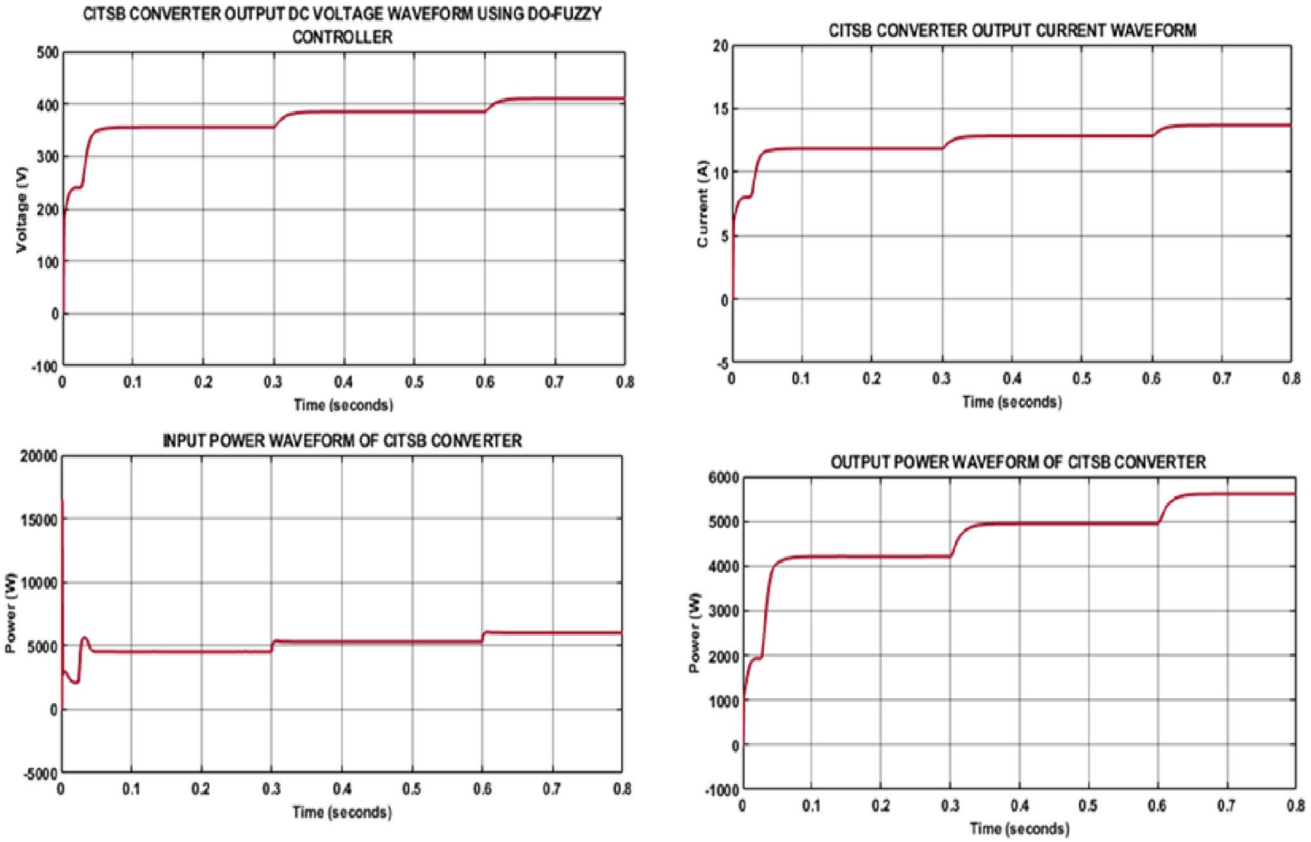

Fig. 19 Converter Output and Power Waveform Under Test Case 3

Fig. 20 PV Panel Profile Under Test Case 4

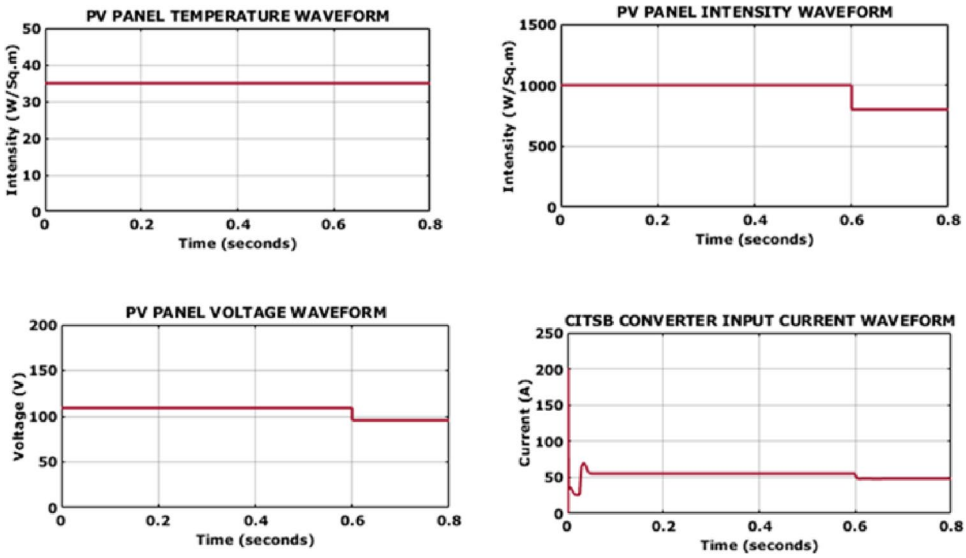

output THD waveform under grid conditions with a 1500 W power supply is shown in the Fig. 25, showing a reduced value of 1.90%.

The THD waveform for grid voltage for both 1500KW and 200KW is represented in Fig. 26 under load operating conditions, which clearly shows 0.00% of THD value.

4.7 Hardware Analysis

Figure 27 indicates the designed PV-tied grid system equipped with a CITSB converter. The system integrates a DOF based MPPT for enhanced performance. The setup ensures improved tracking speed, power system stability, demonstrating the robustness of developed control

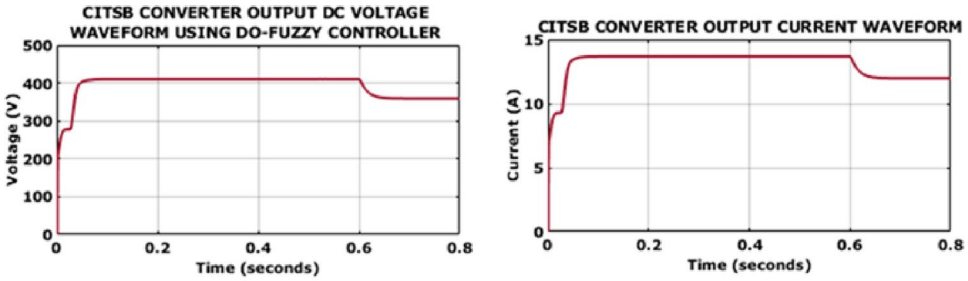

Fig. 21 Converter Output and Power Waveform under Test Case 4

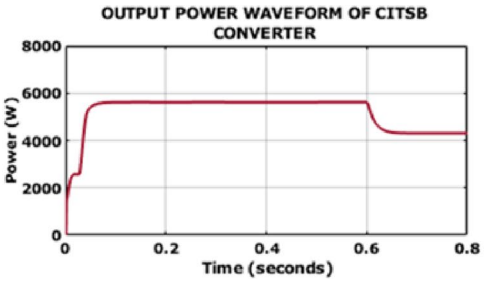

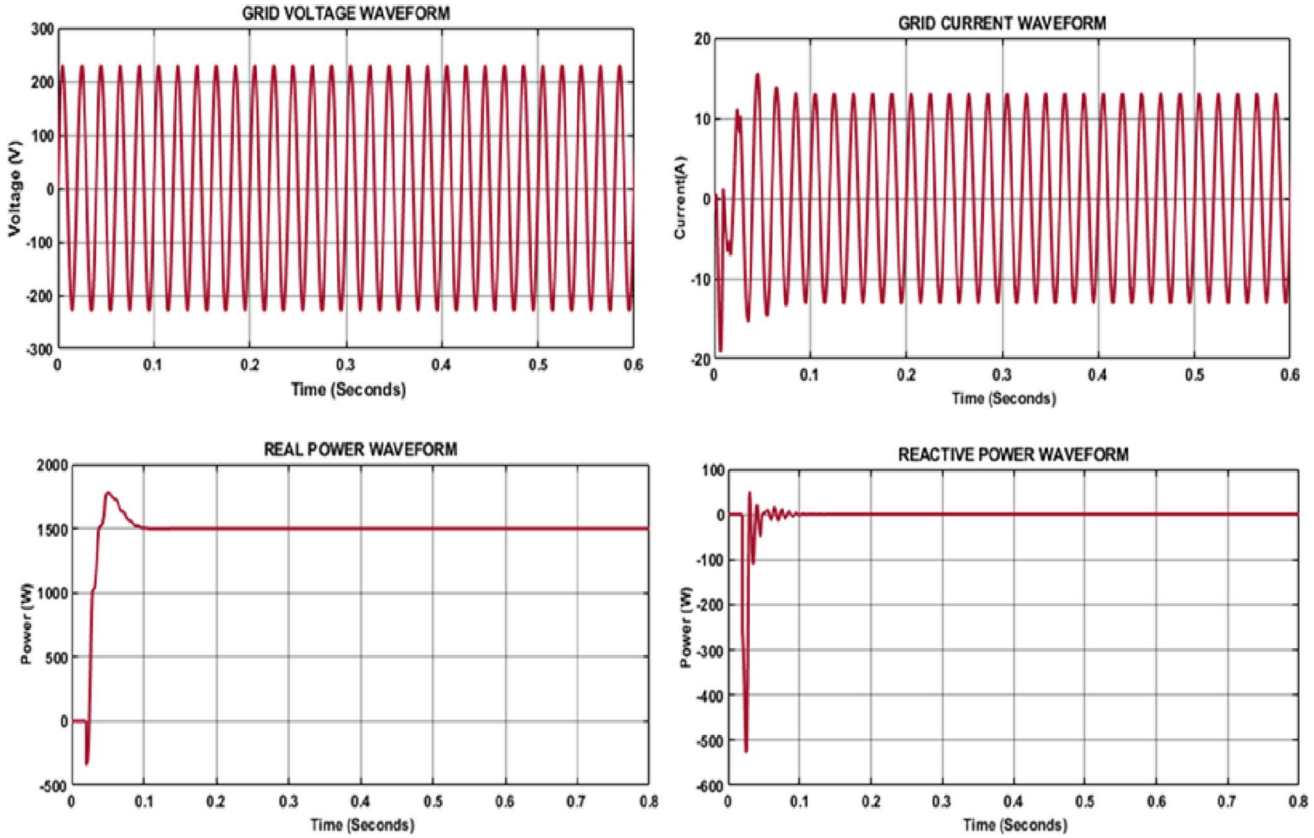

Fig. 22 Output Waveforms for Grid Performance under 1500 W

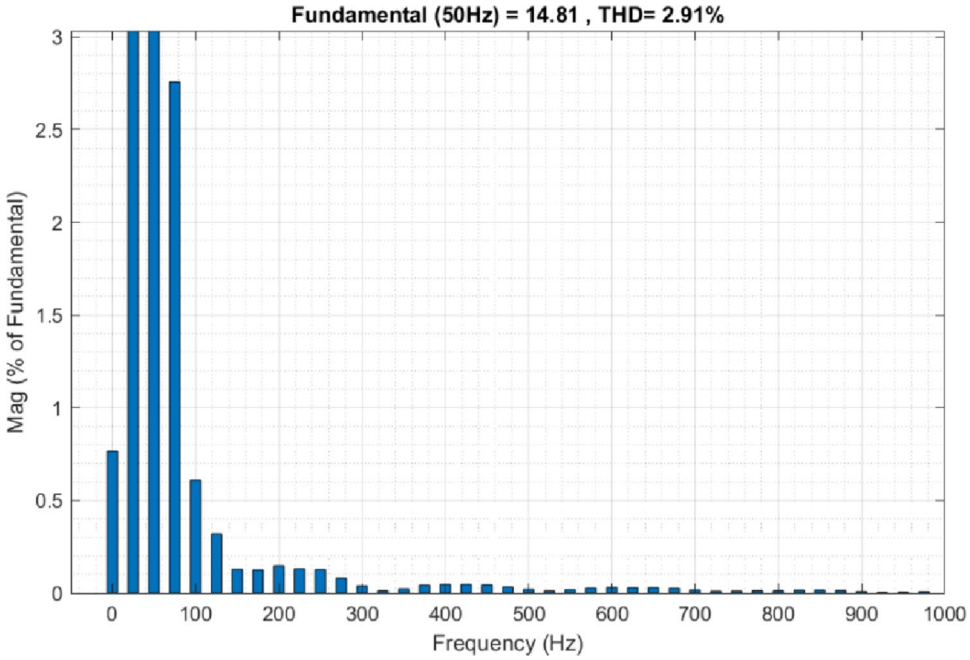

Fig. 23 THD Waveform under 1500 W Power Supply

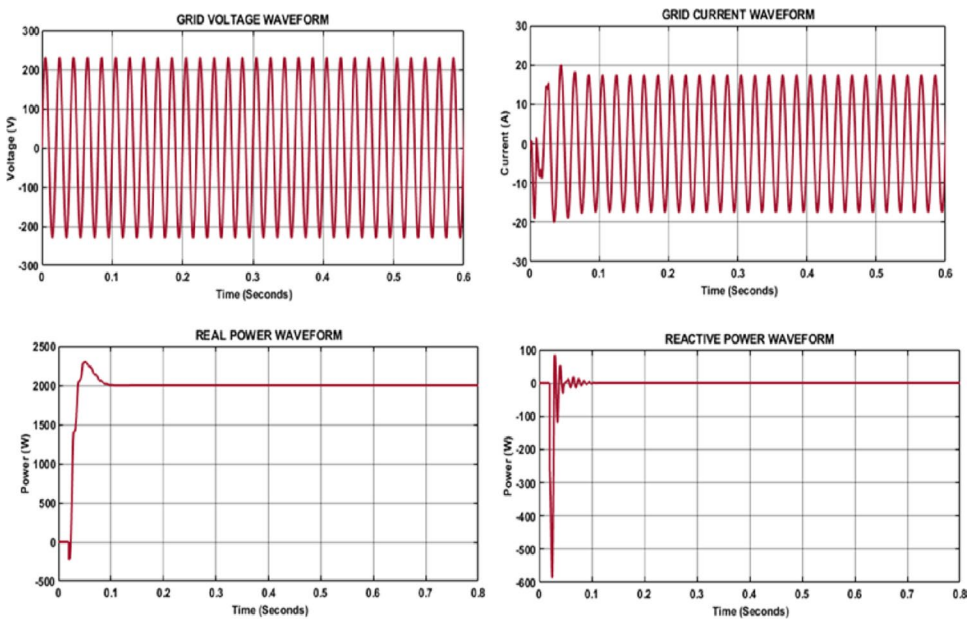

Fig. 24 Output Waveforms for Grid Performance Under 2000 W

strategy in practical grid integrated PV applications. Table 3 showcases the components specifications of experimental prototype.

The converter's performance is demonstrated in the Fig. 28, showing a clear voltage step-up operation. The input voltage waveform remains stable around 120 V, indicating a consistent supply to the converter. On the output side, the voltage is successfully boosted to 400 V with minimal ripple, showcasing efficient conversion capability.

According to Fig. 29, the grid resultant profile ensures the consistent voltage 230 V together with 12 A current value is kept preserved accordingly. These results assure that the system delivers a stable and reliable power output, ensuring compatibility with grid standards.

The THD waveforms for two power levels 1500 W and 2000 W are illustrated in the Fig. 30. At 1500 W, the THD is measured at 3.76%, while at 2000 W it decreases to 2.40%, indicating improved power quality. The significant reduction in THD at higher power levels reflects the performance of inverter control strategy in suppressing harmonics during increased power delivery.

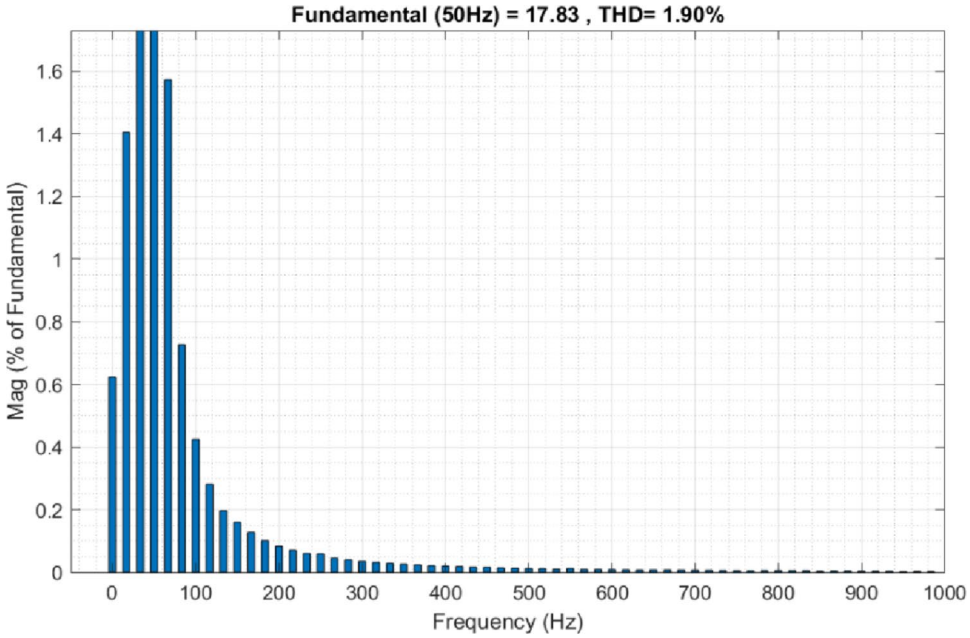

Fig. 25 THD Waveform under 2000 W Power Supply

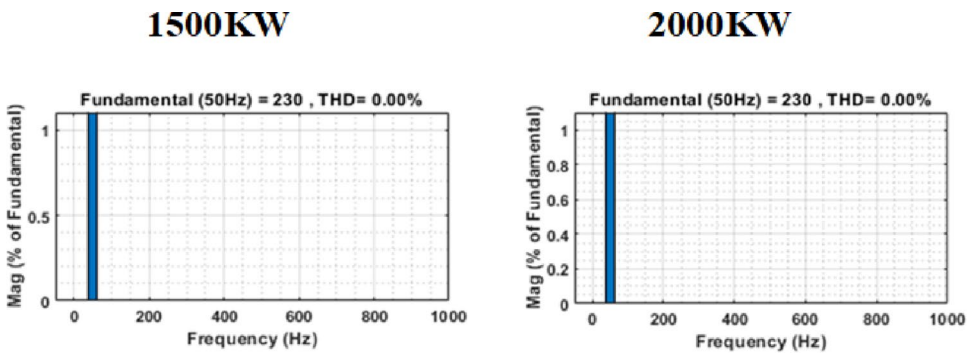

Fig. 26 THD Waveform Under 1500KW and 2000 W Power Supply

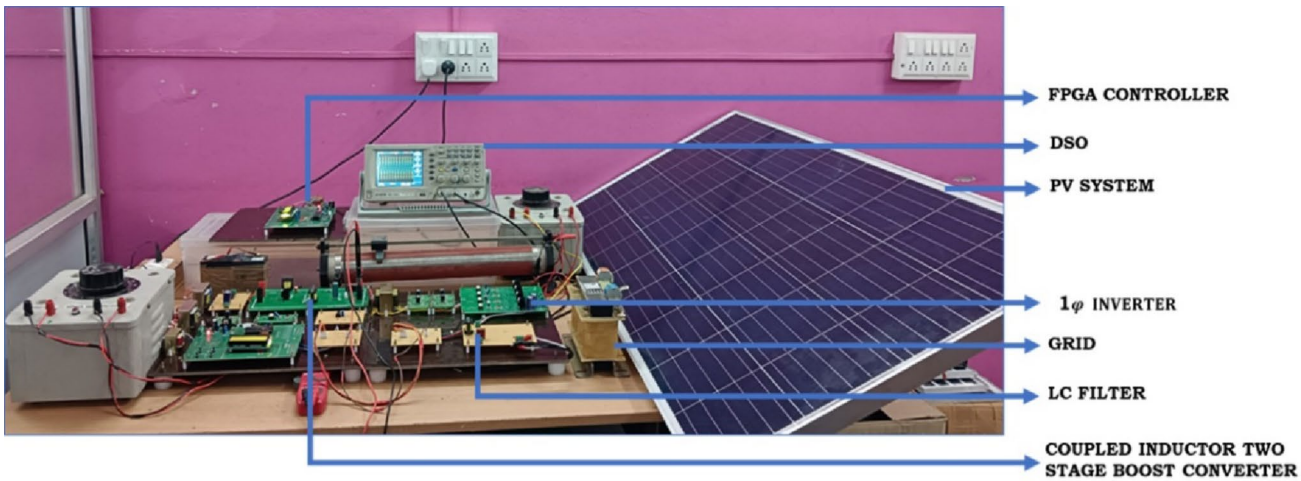

Fig. 27 Hardware Prototype

Table 3 Hardware Prototype

Technical parameter	Specifications
Solar Panel	10
Maximum Power	$250W$
Tolerance	$\pm 3\%$
Series fuse rating	$15A$
Module Efficiency	15.3%
weight	$17kg$
Dimensions	$1650mm \times 992mm \times 40m$
Terminal Box	*IP*65
Maximum system voltage	1000 V DC
Solar cell Efficiency	17.2%
Operating Temperature	$-40^{\circ}\,C - 85^{\circ}\,C$
MPP Voltage V_{MPP}	$27V$ *to* $31V$
MPP Current I_{MPP}	$8A$ *to* $9.2A$

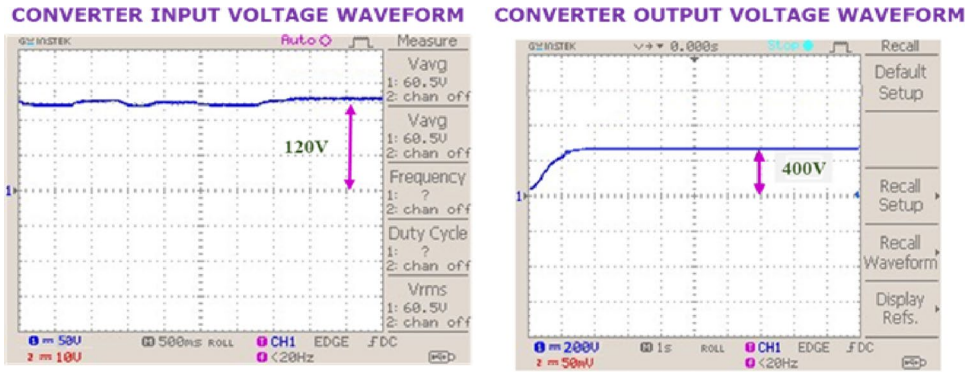

Fig. 28 CITSB Converter Output Waveforms

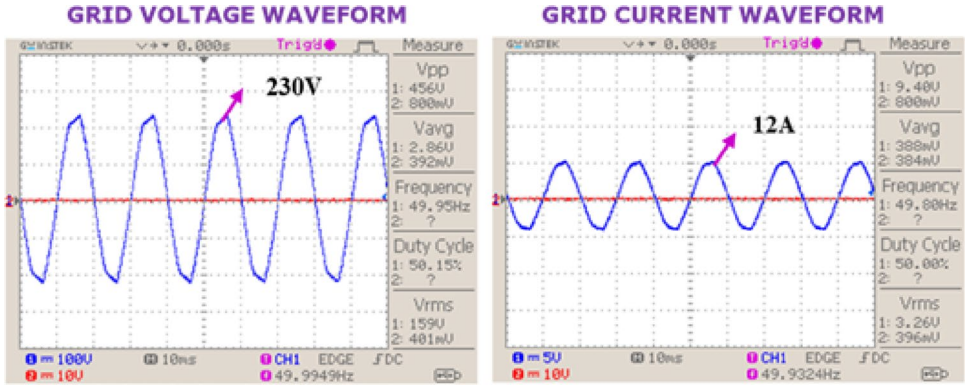

Fig. 29 Grid Output Waveforms

4.8 Comparison Analysis

$$[A] \rightarrow [41],\ [B] \rightarrow [42],\ [C] \rightarrow [43],$$
$$[D] \rightarrow [44]\ and\ Proposed\ converter \rightarrow CITSB\ Converter$$

The key parameters including reactive and active components, total component count, efficiency, voltage gain, and output configuration are highlighted in Table 4 comparative analysis of different converters. With a grounded output, the designed CITSB Converter has better outcomes than [A-Andrade AM et al 2019], [B-Hasanpour S et al 2019], [C-Moradpour R et al 2018], [D-Zheng Y et al 2019] with regard to efficiency, reaching 98.2%. Additionally, it balances moderate component utilization with greater voltage gain. The voltage gain comparison illustrated in Fig. 31, from the graph observation, the designed CITSB converter has improved gain ration compared to other approaches reported in [A-D].

A comparison of different MPPT controllers according to tracking efficiency, time and complexity is showcased in Table 5. With the lowest complexity and the fastest tracking

Fig. 30 THD Waveforms

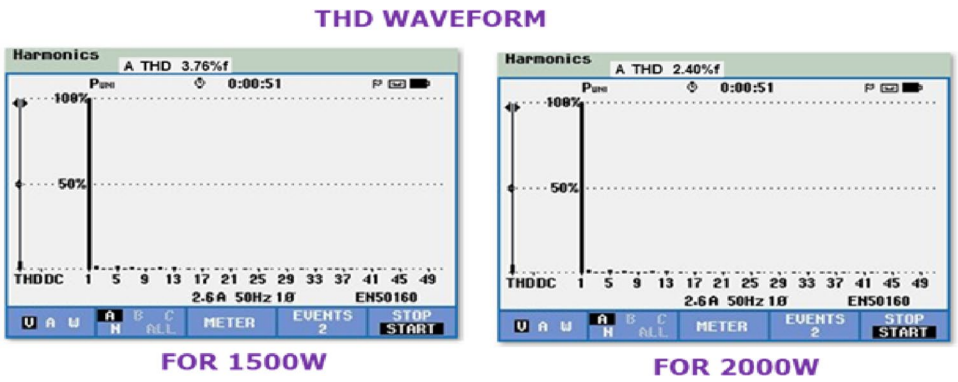

Table 4 Comparative Evaluation of Converters

Converter	Reactive Components		Active Components		Total Count	Efficiency (%)	Voltage Gain (M)	Output port
	CL	C	D	S				
Hybrid High Step Up Boost [A]	2	8	8	1	19	95.1%	$\frac{4+n_2(2-D)-D}{1-D}$	Grounded
Modified SEPIC [B]	2	5	4	1	12	96.6%	$\frac{1+D\ n_2(2-D)}{(1-D)}$	Grounded
Coupled Inductor Boost [C]	2	5	4	1	12	94%	$\frac{2+n_2+D}{(1-D)}$	Grounded
SC based Boost [D]	2	3	2	1	8	93.8%	$\frac{1+(n_2+1)D}{(1-D)}$	Grounded
CITSB Converter	2	5	5	1	13	98.2%	$\frac{2+n+nD}{1-D^2}$	Grounded

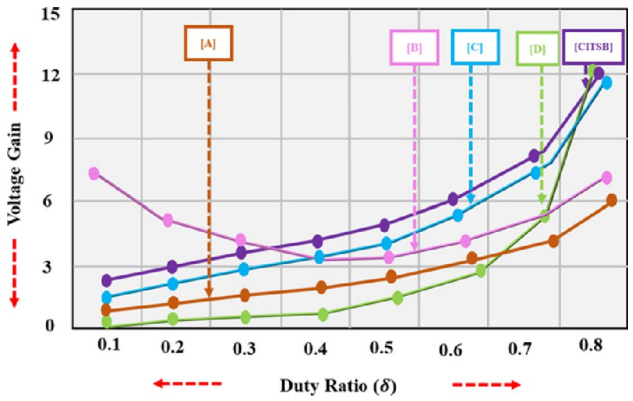

Fig. 31 Voltage Gain Comparison

time (3.1s) and best efficiency (99.6%), the developed MPPT performs better than the others. Strong performance and low complexity are also demonstrated by conventional fuzzy MPPT. Higher complexity is seen in the controllers in (Laxman et al. 2021; Andrade et al. 2019; Hasanpour et al. 2019), with (Hasanpour et al. 2019) having the highest efficiency of all with a tracking time of 4.1s and 98.7%.

An examination of different MPPT controllers is shown in Table 6. With the highest power output of 5000 W and an efficiency of 99.6%, the promoted DOA-FLC approach performs better than the others. Traditional techniques, such as P&O and INC, provide slower tracking and less power. While FLC and NN perform better, they are still inferior to DOF-MPPT with regard to output power, tracking efficiency and tracking speed.

The radar chart in Fig. 32 compares the MPPT methods including P&O, INC, FLC, and the proposed DOA-FLC—across tracking efficiency, convergence time, voltage ripple, and current ripple. DOA-FLC demonstrates superior performance with the highest efficiency, minimal ripples, and fastest response time.

The power oscillation comparison showcased in Fig. 33 represents that the proposed DOA_FLC MPPT exhibits the minimum power oscillations in both simulation and hardware outcomes in contrasted with other traditional approaches. This close agreement between simulation and experimental results confirms that improved stability performance.

5 Conclusion

This research develops a design, simulation and hardware implementation of a high-performance PV tied grid system integrating a CITB converter with a DOA tuned FLC method for MPPT. The simulation studies validate the superiority of developed configuration in terms of voltage gain, efficiency and dynamic response in contrasted to classical controller and converter combinations. The CITSB converter demonstrates a high conversion efficiency of 98.2% along with grounded output and optimized component count,

Table 5 Comparison of MPPT controllers

MPPT Approaches			Input Parameters	Published Year
Improved PSO MPPT Controller (Sangrody et al. 2023)	Tracking Time (s)	4.5s	V_{PV}, I_{PV}	2023
	Tracking Efficiency (%)	97.3%		
	Complexity	High		
Sliding Mode with PSO MPPT controller ([janssou et al. 2021)	Tracking Time (s)	4.9s	V_{PV}, I_{PV}	2021
	Tracking Efficiency (%)	96.4%		
	Complexity	High		
Hierarchical Pigeon MPPT controller (Zhao et al. 2021)	Tracking Time (s)	4.1s	V_{PV}, I_{PV}	2021
	Tracking Efficiency (%)	98.7%		
	Complexity	Medium		
Conventional Fuzzy MPPT	Tracking Time (s)	3.9s	V_{PV}, I_{PV}	-
	Tracking Efficiency (%)	97.6%		
	Complexity	Low		
Proposed MPPT	Tracking Time (s)	3.1s	V_{PV}, I_{PV}	–-
	Tracking Efficiency (%)	99.6%		
	Complexity	Low		

Table 6 valuation of MPPT controllers

MPPT Method	Tracking Speed (sec)	Power at MPP (W)	Current at MPP (A)	Voltage at MPP (V)	Tracking Efficiency (%)
P&O [29]	0.10	240.4	2.94	81.63	96.1%
INC [30]	0.9	241	2.93	82.01	97.2%
NN [32]	0.7	241	2.93	82.01	97.8%
FLC	0.5	500	4.56	83.23	98.3%
DOA-FLC (Proposed)	0.3	5000	8.35	29.95	99.6%

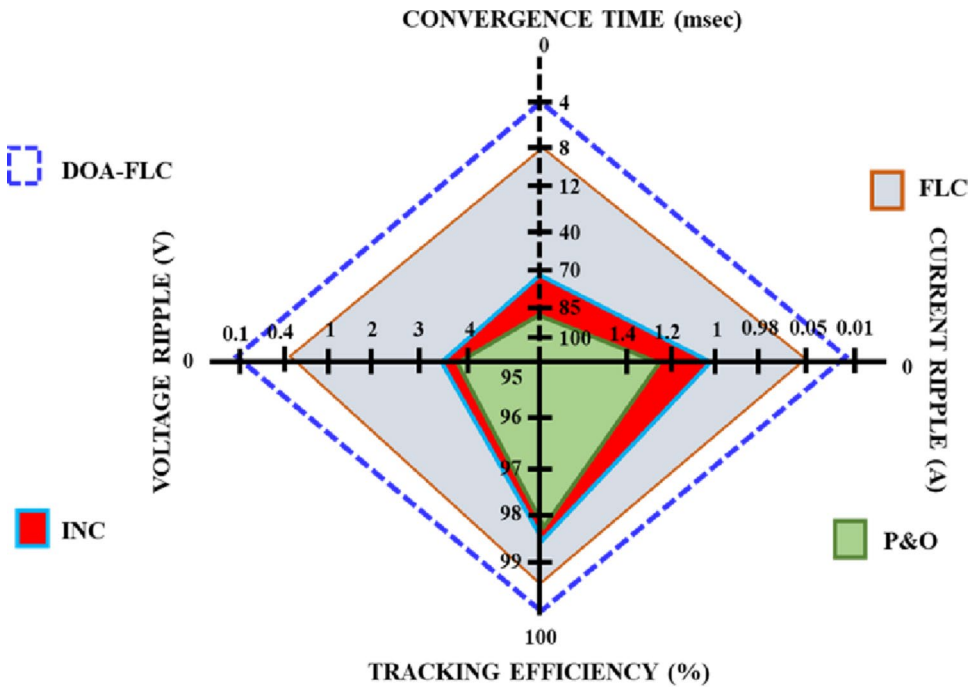

Fig. 32 Performance Evaluation

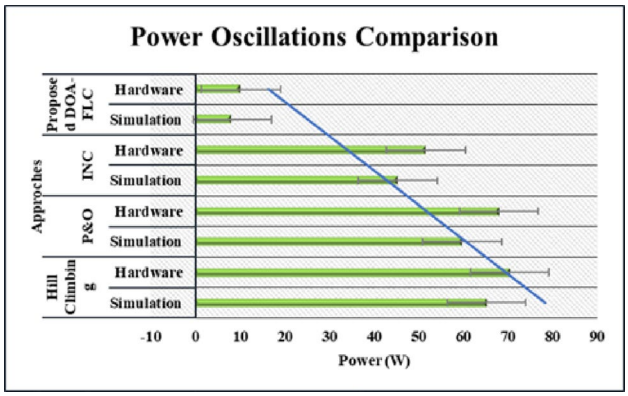

Fig. 33 Power Oscillation Comparison

confirming its suitability for grid connected PV applications. The effectiveness of proposed MPPT strategy is evidenced through both simulation and experimental outcomes. The DOA tuned FLC achieves a fast-tracking time of 0.3s, extracts up to 5000 W, and attains a tracking efficiency of 99.6%, outperforming traditional P&O, INC, NN and traditional FLC methods. Hardware validation further confirms close agreement with simulation outcomes, demonstrating stable operation, reduced oscillations around the MPP and reliable real time performance at changing circumstances. In summary, the combined simulation and hardware results highlight the practical implementation contribution of this work, proving that the developed system offers an efficient, robust and deployable solution for enhanced energy harvesting in modern PV based grid applications.

Author Contributions **Conceptualization: ** Narayanan Rishikesh, **Data Curation: ** Narayanan Rishikesh**Project administration: ** Jeyaraj Senthil Kumar, N. Janaki**Supervision: ** Jeyaraj Senthil Kumar, N. Janaki**Validation: ** Jeyaraj Senthil Kumar, N. Janaki**Writing-original draft: ** Narayanan Rishikesh**Writing-review & editing: ** Jeyaraj Senthil Kumar, N. Janaki & Narayanan Rishikesh.

Funding The authors received no specific funding for this study.

Data Availability Data is contained within the article.

Declarations

Competing Interests The authors declare no competing interests.

Ethics Approval Not applicable.

Consent for Publication Not applicable.

References

Ali ZM, Alquthami T, Alkhalaf S, Norouzi H, Dadfar S, Suzuki K (2022) Novel hybrid improved Bat algorithm and fuzzy system based MPPT for photovoltaic under variable atmospheric conditions. Sustain Energy Technol Assess 52:102156

Aly M, Rezk H (2021) A MPPT based on optimized FLC using Manta ray foraging optimization algorithm for thermo-electric generation systems. Int J Energy Res 45(9):13897–13910

Andrade AM, Schuch L, da Silva Martins ML (2019) Analysis and design of high-efficiency hybrid high step-up DC-DC converter for distributed PV generation systems. IEEE Trans Ind Electron 66(5):3860–3868

Azab M (2021) A finite control set model predictive control scheme for single-phase grid-connected inverters. Renew Sustain Energy Rev 135:110131

Babu N, Guerrero JM, Siano P, Peesapati R, Panda G (2020) An improved adaptive control strategy in grid-tied PV system with active power filter for power quality enhancement. IEEE Syst J 15(2):2859–2870

Badoni M, Singh A, Singh AK, Saxena H, Kumar R (2021) Grid tied solar PV system with power quality enhancement using adaptive generalized maximum versoria criterion. CSEE J Power Energy Syst 9(2):722–732

Bairwa AK, Joshi S, Singh D (2021) Dingo optimizer: a nature-inspired metaheuristic approach for engineering problems. Math Probl Eng 2021(1):2571863

Bao D, Kumar A, Pan X, Xiong X, Beig AR, Santosh Kumar Singh (2021) Switched inductor double switch high gain DC-DC converter for renewable applications. IEEE Access 9:14259–14270

Bhattacharyya S, Samanta S, Mishra S (2020) Steady output and fast tracking MPPT (SOFT-MPPT) for P&O and inc algorithms. IEEE Trans Sustain Energy 12(1):293–302

Dhimish M, Schofield N (2022) Single-switch boost-buck DC-DC converter for industrial fuel cell and photovoltaics applications. Int J Hydrog Energy 47(2):1241–1255

Fan X, Sun H, Yuan Z, Li Z, Shi R, Ghadimi N (2020) High voltage gain DC/DC converter using coupled inductor and VM techniques. IEEE Access 8:131975–131987

Firdausi AA, Cunard RT, Agustin EI, Nahdliyah SD, Nugroho TA (2020) An improved control for MPPT based on FL-PSo to minimize Oscillation in photovoltaic system. Int J Pow Elec Dri Syst 8694:1083

Gulzar MM, Iqbal A, Sibtain D, Khalid M (2023) An innovative converterless solar PV control strategy for a grid connected hybrid PV/wind/fuel-cell system coupled with battery energy storage. IEEE Access 11:23245–23259

Gupta AK, Patari RK, Amity T, Chauhan YK, Machala OP, Khan B, Gupta PK (2020) Effect of various incremental conductance MPPT methods on the charging of battery load feed by solar panel. IEEE Access 9:90977–90988

Hasanpour S, Baghramian A, Mojallali H (2019) A modified SEPIC-based high step-up DC-DC converter with quasi-resonant operation for renewable energy applications. IEEE Trans Ind Electron 66(5):3539–3549

Ibrahim MH, Ang SP, Dani MN, Rahman MI, Petra R, Sulthan SM (2023) Optimizing step-size of perturb & observe and incremental conductance MPPT techniques using PSO for grid-tied PV system. IEEE Access 11:13079–13090

Imanlou A, Najmi ES, Behkam R, Nazari-Heris M, Gharehpetian GB (2023) A new high voltage gain active switched-inductor based high step-up DC–DC converter with coupled-inductor. IEEE Access 11:56749–56765

janssou DM, Dadjé A, Tom A, Djongyang N (2021) Improvement of the dynamic response of robust sliding mode MPPT Controller-Based PSO algorithm for PV systems under Fast-Changing atmospheric conditions. Int J Photoenergy 1:6671133

Kavin KS, Subha Karuvelam P, Devesh Raj M, Sivasubramanian M (2024) A novel KSK converter with machine learning MPPT for PV applications. Electr Power Compon Syst. 1–19

Kavin KS, Subha Karuvelam P, Matcha M, Vendoti S (2025) Improved BRBFNN-based MPPT algorithm for coupled inductor KSK converter for sustainable PV system applications. Electrical Engineering, vol. 107, no. 6, pp. 7831–7853.

Khan S, Zaid M, Mahmood A, Nooruddin AS, Ahmad J, Alghaythi ML, Alamri B, Tariq M, Sarwar A, Lin CH (2021) A new transformerless ultra high gain DC–DC converter for DC microgrid application. IEEE Access 9:124560–124582

Kiran SR, Basha CH, Singh VP, Dhanamjayulu C, Prusty BR, Khan B (2020) Reduced simulative performance analysis of variable step size ANN based MPPT techniques for partially shaded solar PV systems. IEEE Access 10:48875–48889

Kokkonda K, Kulkarni PS (2021) A high gain soft-switching active-clamped coupled-inductor-based converter for grid-tied photovoltaic applications. Electr Eng 10(6):2783–2797

Kumar GG, Sundaramoorthy K, Karthikeyan V, Babaei E (2020) Switched capacitor–inductor network based ultra-gain DC–DC converter using single switch. IEEE Trans Industr Electron 67(12):10274–10283

Kumar MA, Krishnasamy V (2022) Enhanced quadratic boost converter based on voltage lift technique for fuel cell powered electric vehicle. Comput Electr Eng 102:108256

Kumar M, Yadav VK, Verma AK (2023) Switched capacitor based high gain boost converter for renewable energy application. IEEE J Emerg Sel Top Industrial Electron 4(3):818–826

Kurian GM, Jeyanthy PA, Devaraj D (2022) FPGA implementation of FLC-MPPT for harmonics reduction in sustainable photovoltaic system. Sustain Energy Technol Assess 52:102192

Lakshmi D, Sathishkumar S, Sreedhar R, Vasumathi G, Md Mujahid Irfan Md, Balasubramanian M (2025) Enhanced Solar PV System with Battery Storage and Grid Integration Using Cascaded ANFIS-Based MPPT and Self-Lift Luo Converter. In 2025 3rd International Conference on Device Intelligence, Computing and Communication Technologies (DICCT) 361–366. IEEE

Laxman B, Annamraju A, Srikanth NV (2021) A grey Wolf optimized fuzzy logic based MPPT for shaded solar photovoltaic systems in microgrids. Int J Hydrog Energy 46(18):10653–10665

Li B, Wang P, Wang Z, Ma X, Bi H (2021) A new coupled-inductor-based high-gain interleaved DC-DC converter with sustained soft switching. IEEE Trans Veh Technol 70(7):6527–6541

Mishra PK, Tiwari P (2021) Incremental conductance MPPT in grid connected PV system. Int J Eng Sci Technol 13(1):138–145

Mohammed S, Sheik D, Devaraj, Imthias Ahamed TP (2021) GA-optimized fuzzy-based MPPT technique for abruptly varying environmental conditions. J Institution Eng (India): Ser B 102(3):497–508

Mohseni P, Mohammad salehian S, Islam MR, Muttaqi KM, Sutanto D, Alavi P (2021) Ultrahigh voltage gain DC–DC boost converter with ZVS switching realization and coupled inductor extendable voltage multiplier cell techniques. IEEE Trans Industr Electron 69(1):323–335

Moradpour R, Ardi H, Tavakoli A (2018) Design and implementation of a new SEPIC-based high step-up DC/DC converter for renewable energy applications. IEEE Trans Ind Electron 65(2):1290–1297

Naqvi SB, Kumar S, Singh B (2020) Three-phase four-wire PV system for grid interconnection at weak grid conditions. IEEE Trans Ind Appl 56(6):7077–7087

Rahimi R, Habibi S, Ferdowsi M, Shamsi P (2021) Z-source-based high step-up DC–DC converters for photovoltaic applications. IEEE J Emerg Sel Top Power Electron 10(4):4783–4796

Rao BT, De D (2023) A coupled inductor-based high-gain ZVS DC–DC converter with reduced voltage stresses. IEEE Trans Power Electron 38(12):15956–15967

Rasheed MS, Shihab S (2020) Modelling and parameter extraction of PV cell using single-diode model. Adv Energy Convers Mater, 109–119

Rezk H, Aly M, Ghoniem RM (2023) Robust fuzzy logic MPPT using gradient-based optimization for PEMFC power system., Sust Rezk H, Aly M, Ghoniem RM ainability, 15(18), 13368.

Sadaf S, Bhaskar MS, Meraj M, Iqbal A, Al-Emadi N (2020) A novel modified switched inductor boost converter with reduced switch voltage stress. IEEE Trans Industr Electron 68(2):1275–1289

Sangrody R, Taheri S, Cretu AM, Pouresmaeil E (2023) An improved PSO-based MPPT technique using stability and steady state analyses under partial shading conditions. IEEE Trans Sustain Energy 15(1):136–145

Shanthi T, Prabha SU, Sundaramoorthy K (2021) Non-isolated n-stage high step-up DC-DC converter for low voltage DC source integration. IEEE Trans Energy Convers 36(3):1625–1634

Sorte P, Kishor KP, Panda, Panda G (2021) Current reference control based MPPT and investigation of power management algorithm for grid-tied solar PV-battery system. IEEE Syst J 16(1):386–396

Sreedhar R, Karunanithi K, Ramesh S, Raja SP, Naresh Kumar P (2025) Optimizing grid connected photovoltaic systems using elementary LUO converter and GWO-RBFNN based MPPT. Electr Eng 107(2):2297–2313

Veerachary M, Kumar N (2020) Analysis and design of quadratic following boost converter. IEEE Trans Ind Appl 56(6):6657–6673

Venkatanarayana B, Rosalina KM (2024) A new MPPT mechanism based on multi-verse optimization algorithm tuned FLC for photovoltaic systems. Sci Rep 14(1):28066

Wu X, Yang M, Zhou M, Zhang Y, Fu J (2020) A novel high-gain dc-dc converter applied in fuel cell vehicles. IEEE Trans Veh Technol 69(11):12763–12774

Xue C, Wu X, Li Y (2024) Virtual reduced-order plant-based speed sensorless control for AC motor drives with output LC filter. In: 2024 IEEE Applied Power Electronics Conference and Exposition (APEC), 1035–1040.

Yan D, Yin H, Li T, Ma C (2021) A two-stage scheme for both power allocation and EV charging coordination in a grid-tied PV–battery charging station. IEEE Trans Industr Inf 17(10):6994–7004

Zhang Y, Wang YJ, Zhang Y, Yu T (2022) Photovoltaic fuzzy logical control MPPT based on adaptive genetic simulated annealing algorithm-optimized BP neural network. Processes 10(7):1411

Zhao Z, Zhang M, Zhang Z, Wang Y, Cheng R, Guo J, Yang P, Lai CS, Li P, Lai LL(2021)Hierarchical pigeon-inspired optimization-based MPPT method for photovoltaic systems under complex partial shading conditions. IEEE Trans Industr Electron. 69(10), 10129–10143.

Zheng Y, Smedley KM (2019) Analysis and design of a single-switch high step-up coupled-inductor boost converter. IEEE Trans Power Electron 35(1):535–545